Measurement 222 (2023) 113500

Contents lists available at ScienceDirect

Measurement

journal homepage: www.elsevier.com/locate/measurement

Precise measurement method of carrier motion state in microgravity environment

Mingyue Liu [a], Huizhong Zhu [a,*], Xinchao Xu [a,b], Youqing Ma [b], Shuo Zhang [b], Junbiao Wang [c]

[a] School of Geomatics, Liaoning Technical University, Fuxin 123000, China
[b] Aerospace Information Research Institute, Chinese Academy of Sciences, Beijing 100094, China
[c] National Microgravity Laboratory, Institute of Mechanics, Chinese Academy of Sciences, Beijing 100190, China

ARTICLE INFO

Keywords:
Multi-camera calibration
Stereo vision
Extraction of homonymous points
Random Sample Consensus (RANSAC)
Carrier motion state

ABSTRACT

In the field of aerospace and planetary science, precise measurement of the motion state of a moving carrier represents an important part of scientific exploration missions. the paper presents a fusion of the stereo vision and IMU to measure the velocity, angle, and angular velocity of a moving carrier precisely. First, a stereo camera self-calibration model with additional geometric constraints is developed, which accuracy of better than 0.379 pixels is achieved. Then, a three-dimensional reconstruction with accuracy of better than 0.727 pixels is achieved. Finally, the spatial relationship between the carrier, the stereo camera, and the IMU is used to determine the absolute pose change of the moving carrier relative to the center of the Earth. The proposed method ensures high measurement accuracy of the velocity, angle, and angular velocity of the moving carrier of better than 0.19 mm/s, 0.09°, and 0.127°/s, respectively, which can provide reliable technical support for the motion state estimation of deep space moving vehicles.

1. Introduction

With the progress of science and technology, the application of intelligence in fields such as aerospace, industrial design, and autonomous driving has greatly promoted the rapid development of smart city construction [1–4]. The motion pose of the carrier represents important data reflecting the motion state of the carrier, having high guiding significance for the test identification of the carrier, industrial design, and aerospace development [5–7]. In the process of performing deep space exploration missions, the accurate measurement of the motion state of the spacecraft plays an important role in tasks such as relative navigation, rendezvous and docking, and lander control. there are high requirements on the state vectors of the spacecraft's pose angle and attitude pose velocity, which focus on improving the robustness, agility and accuracy of the state vector. the precise star sensor can use its own circuit structure to determine the pose of satellites and spacecraft by detecting stars in different positions on the planet, and provide the three-axis pose of the spacecraft relative to the inertial coordinate system. However, the measurement environment of the star sensor is relatively complex, and the internal electromagnetic wave environment will affect the measurement results, resulting in a certain deviation between the actual measurement posture of the spacecraft and the ideal spacecraft measurement results, and the measurement stability needs to be strengthened[8–12]. Therefore, for on-orbit conditions, a stable and reliable carrier pose measurement scheme is of great significance.

According to the operational method type, the pose parameter measurements of a moving carrier can be roughly divided into two categories: the pose parameter measurement of the cooperative carrier and the pose parameter measurement of the non-cooperative carrier [13]. The former refers to setting targets on a moving carrier and obtaining the carrier's pose parameters based on the known position information on the target feature points. Meanwhile, the latter does not need a target, and uses photoelectric, electromagnetic, visual, and other sensor technologies to extract the characteristics of a motion carrier and employs stereo vision measurement techniques, motion image analysis methods, and other methods to obtain the carrier's pose parameters. A cooperative carrier method requires using auxiliary devices, such as cooperative signs or communication lines, whereas a non-cooperative carrier method lacks mutual communication between sensors; therefore, the cooperative carrier methods have higher measurement accuracy than the non-cooperative carrier methods.

Extensive research work has been conducted on the motion carrier pose measurement technology. The existing measurement methods can be mainly divided into visual measurement methods [14], laser tracking

* Corresponding author.
E-mail address: zhuhuizhong@whu.edu.cn (H. Zhu).

https://doi.org/10.1016/j.measurement.2023.113500
Received 17 July 2023; Received in revised form 22 August 2023; Accepted 28 August 2023
Available online 2 September 2023

measurement methods [15], and measurement methods based on deep learning [16].

The visual measurement methods use the mapping relationship between the carrier in the three-dimensional (3D) space and a two-dimensional (2D) image and calculate the geometric size, spatial position, and pose of the carrier based on the image features. These methods have been widely used in the fields of part detection, deformation measurement, equipment assembly, rendezvous and docking, and integrated navigation due to their advantages of being non-contact, high precision, and fast speed [17]. In [18], a monocular vision measurement scheme for the measurement of the size, spatial position, and status of static carriers was proposed. For the pose measurement of a dynamic carrier, in [19], a monocular vehicle pose estimation algorithm was combined with the 3D model of a vehicle; this method can realize the pose estimation of a vehicle, but it is limited by the 3D model of the carrier. In [20], the authors developed a monocular vision-based pose measurement method for the air-floating platform. By laying out non-coplanar targets as feature points, the pose information on the air-floating platform was obtained by an iterative least squares pose estimation algorithm. However, this method requires designing the corresponding target shape and layout according to the shape of the air-bearing table, and the pose estimation process is relatively complex, but the application scenario is relatively simple. In [21], a single-axis high-precision rotating platform was combined with a camera to measure the pose of the spacecraft. However, due to the single-degree-of-freedom rotating platform and the sticking target method, there are limitations on the measurement range and non-cooperative measurement. Further, in [22], a pose estimation method based on a TOF camera, which can avoid the defect of sticking targets, was proposed, and typical components on the carrier were used to perceive the pose evolution of the carrier, which works well in simulated environments. Furthermore, in [23], the authors proposed a method based on feature information fusion, which realizes positioning by detecting feature information on the carrier. However, this method has a high time complexity, and its detection accuracy is affected by illumination. Reference [24] used the stereo camera to measure the state of a moving carrier and clustered the dynamic carrier segmentation. According to the optimization methods of overlapping the view area local constraints and the global closed loop, the overall 3D model of a carrier was constructed, and accurate pose measurement was realized. To sum up, the monocular measurement methods have the characteristics of a simple structure, but they have limitations on the carrier model. The stereo measurement methods can complete 3D reconstruction, but they are restricted by the carrier feature points, which increases the time cost of the calculation process [25].

Laser tracking-based measurement technology uses lidar to obtain point cloud data and realizes the pose measurement of moving carriers by processing the point cloud data. This measurement technology belongs to the class of high-precision spatial information acquisition methods. Due to the advantages of high measurement accuracy, fast speed, and wide measurement range, this technology has been widely used in many fields, including high-end intelligent manufacturing and large-scale scientific engineering. In [26], the authors proposed to calculate the relative pose by searching congruent tetrahedrons directly based on the scanned point cloud data and model point cloud data. Since pure-laser point cloud data are greatly affected by the environmental parameters and lack texture information, fusion vision and laser tracking solutions have been usually used to measure the motion state of the carrier. In [27], a pose measurement method that combines a position sensing detector (PSD) and monocular vision was developed, and the total station data were used to measure azimuth and elevation angles. A CCD camera was installed on the total station to project and measure the roll angle, thus overcoming the problems of a slow update rate of the roll angle and a limited measurement range. However, there was redundant information on monocular vision pose measurement. In [28], a method of pose angle measurement using the laser tracking equipment as a base station was proposed, where monocular vision was combined with the corner cube prism and photoelectric position sensor. This method comprehensively used the corner cube and PSD to measure high-resolution yaw angle and pitch angle information, providing a solution to the current domestic laser tracking pose measurement problems. Further, reference [29] introduced a laser tracking pose angle measurement method based on weighted least squares, which combines the high precision of short-distance monocular vision-based measurement and the redundancy of multi-sensor pose measurement information. A mathematical model of pose measurement was established for data fusion, which improved the measurement accuracy of the pose angle. Although the above-mentioned methods can measure the pose of the carrier, the high redundancy of point cloud data and complex installation of fusion equipment lead to the low universality of these methods.

In recent years, the deep learning-based measurement methods of the carrier motion state have achieved noticeable progress. Aiming to solve the problem of spacecraft pose estimation, reference [30] proposed a learning-based spacecraft pose prediction method, which combines the spacecraft detection network (SDN) and keypoint detection network (KDN) detection feature key points, can automatically select high-precision key points by using the key point selection strategies, and employs the EPnP algorithm to estimate the pose of the spacecraft, thus effectively improving the accuracy of the spacecraft pose estimation. In [31], a pose initialization algorithm suitable for different shapes of carrier spacecraft was developed. By searching for convex defection features of a carrier image and combining the corresponding relationship between the 2D and 3D points, the pose was estimated by solving the PnP problem. Meanwhile, a position awareness network (PANet) for spacecraft pose estimation was proposed in [32], but the calculation time of the sub-steps of the key point extraction process and the construction time of a local structure description were too long, making this scheme unsuitable for navigation systems that need to output the pose data in real-time. In [33], the authors constructed a channel squeeze and excitation—lightweight high-resolution network (scSE-LHRNet) by fusing the You Only Look Once v5 (YOLOv5) model and the lightweight high-resolution network (HRNet), which provided real-time recognition and pose estimation of non-cooperative vehicles. Although the aforementioned methods have their own advantages, the construction models based on deep learning (e.g., convolutional neural networks (CNNs)) are highly uncertain due to the effects of the environmental factors and carrier. These models usually consider the Gaussian distribution, which is not suitable for the underlying manifold structure of the posture, and the deep learning-based methods have high requirements for computer performance. When training the network model, real motion posture data are required as training data, which leads to a strong dependence of the final motion pose parameters on the training image set [34].

The difference between the deep space and the ground environment is that there is no gravitational acceleration in deep space. At present, there is relatively little experimental research on the measurement of carrier motion state in microgravity environments by domestic and foreign scholars. Based on the current research methods, the vision-based measurement methods have a simple structure but are limited by the model type. The methods based on laser tracking have high measurement accuracy, but the data processing complexity is high, and these methods are not universal. The deep learning-based methods have high requirements for computer performance, and the final motion pose parameters are highly dependent on the training dataset, which cannot be adapted to all scenarios. Aiming at the shortcomings and limitations of the above-mentioned methods, considering the influence of space magnetic field interference in deep space environment on pose measurement accuracy, the non-contact and non-magnetic field interference of comprehensive visual measurement and the advantage that IMU can provide absolute attitude information. this study proposes a precise measurement method of a vehicle's motion state in a microgravity environment. The proposed method reconstructs high-precision three-

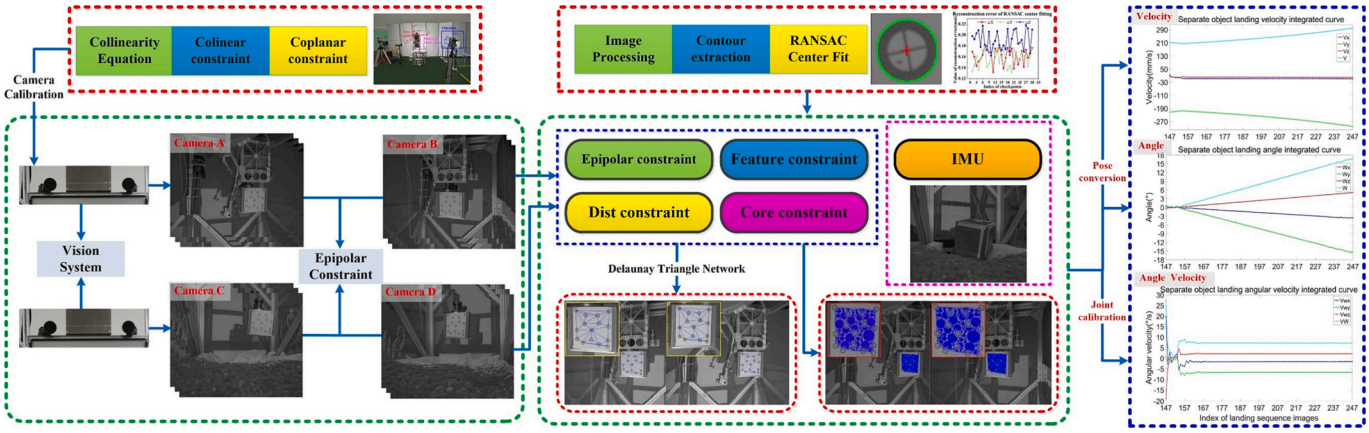

Fig. 1. The block diagram of the proposed method. In Fig. 1, the green dotted frame on the left side of the frame diagram denotes a stereo vision system and sequence images. This part uses a self-checking method with additional geometric constraints to construct a high-precision measurement benchmark; the green frame in the middle represents a circular cooperative target, with the fusion measurement process of 3D high-precision reconstruction, stereo vision, and IMU; the blue block diagram on the right shows the motion state curve of the motion carrier obtained by the proposed method.

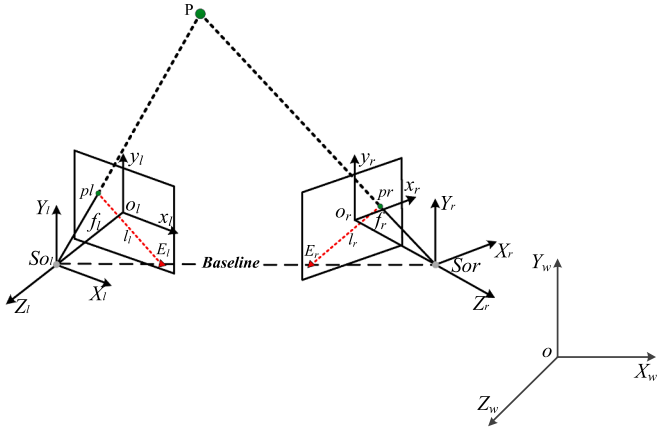

Fig. 2. The stereo camera imaging model; the gray circle denotes the photography center, the green circle refers to the feature image point and the corresponding object space point, the red triangle denotes epipoles, and the red dotted line represents the epipolar line.

dimensional coordinates and determines an absolute pose change of a moving carrier, thereby obtaining reliable movement pose parameters. Meanwhile, it can provide a reference for performance evaluation in navigation control and control devices for deep space exploration.

The main contributions of this study can be summarized as follows:

(1) A measurement platform is constructed to provide high-precision time and space references;
(2) A circular cooperative target is designed, and the center of the circle is fitted with high precision;
(3) A joint camera self-calibration model is constructed to solve the camera parameters;
(4) The absolute pose of the moving carrier relative to the center of the earth is measured by combining stereo vision and IMU.

The remainder of this article is organized as follows. Section 2 describes the overall process of the proposed method and provides a detailed explanation of each part of the proposed method. Section 3 describes the sub-steps of the proposed method, conducts a series of experiments of precise measurement of a moving carrier's state, and analyzes the experimental results. Finally, Section 4 concludes this study.

2. Carrier pose determination method based on fusion of stereo vision and IMU

2.1. Proposed method

Aiming to obtain precise motion state parameters of the carrier in a deep space environment, this paper proposes a precise measurement method that combines stereo vision and IMU. First, 3D high-precision coordinates of a target point are obtained by combining stereo vision, feature point construction, and matching methods. Then to avoid the influence of the external force on the measurement results of a moving carrier, the IMU is combined with a stereo vision for state measurement. The spatial relationships between the carrier, stereo camera, and IMU are used to determine the absolute pose change of the moving carrier relative to the center of the Earth. The proposed carrier pose determination method that combines stereo vision and IMU aims to obtain high-precision, robust, and reliable motion state parameters of a moving carrier in a microgravity environment. The block diagram of the proposed method is shown in Fig. 1. The main parts of the proposed method include stereo camera calibration with additional geometric constraints, the center fitting of feature cooperation targets and 3D coordinate reconstruction data, and a solution to the carrier motion state parameters.

2.2. Camera calibration with additional geometric constraints

First, the initial pose measurement of a moving carrier is realized by using the stereo vision measurement technology. The high-precision camera parameters denote an important benchmark for performing the carrier motion state measurement experiment. Therefore, this paper proposes a camera calibration method with additional geometric constraints.

The geometric structure of a stereo camera is presented in Fig. 2, where $o_l - x_l y_l$ and $o_r - x_r y_r$ are the left and right image plane coordinates, respectively; $S_l - X_l Y_l Z_l$ and $S_r - X_r Y_r Z_r$ are the left and right camera coordinate systems, respectively; $O - X_w Y_w Z_w$ represents the object space coordinate system; f_l and f_r are the focal lengths of the left and right cameras, respectively; B_{lr} is the photographic baseline vector, and its length denotes the distance between the optical centers of the left and right navigation cameras. According to the principle of pinhole imaging, the centers of the left and right cameras, the image point, and the corresponding object space point should be on a straight line; then, in 3D space, lines $\overrightarrow{S_l p_l}$ and $\overrightarrow{S_r p_r}$ will intersect at point P [35]. Points S_l,S_r, and P can determine a plane, which is called the epipolar plane; the intersection points between the $S_l S_r$ and the image plane are epipoles E_l

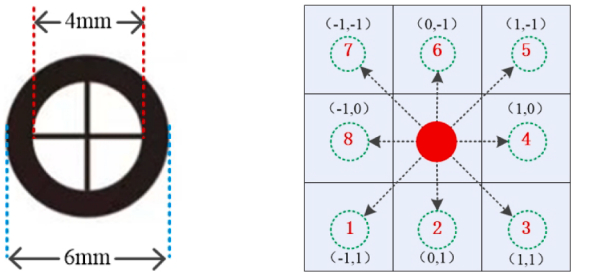

(a) target circle (b) contour tracking

Fig. 3. The schematic diagram of the target circle and contour tracking extraction. The center red-filled circle pixel in (b) can have eight tracking directions; eight dashed arrows represent traceable directions, red numbers denote the direction numbers, and the given coordinates represent the tracking offset.

and E_r, respectively; the intersection line between the polar plane and the two image planes is called the epipolar line.

By performing the perspective projection, the beam adjustment model can be constructed using the projection center, image point, and object space point to solve the camera parameters. The basic expression of this model is as follows[36]:

$$\begin{aligned} x + x_0 + \Delta x &= -f\frac{a_1(X-X_S)+b_1(Y-Y_S)+c_1(Z-Z_S)}{a_3(X-X_S)+b_3(Y-Y_S)+c_3(Z-Z_S)}, \\ y + y_0 + \Delta y &= -f\frac{a_2(X-X_S)+b_2(Y-Y_S)+c_2(Z-Z_S)}{a_3(X-X_S)+b_3(Y-Y_S)+c_3(Z-Z_S)} \end{aligned} \tag{1}$$

where (x, y) denotes the Cartesian coordinates of the image plane; (X, Y, Z) represents the corresponding coordinates under the photogrammetric coordinate system; (X_S, Y_S, Z_S) refers to the three translations in the outer orientation elements; $(a_1, \cdots, c_3)$ is the element of the rotation matrix $\boldsymbol{R}$; (x_0, y_0) is the internal orientation element of the camera; $(\Delta x, \Delta y)$ represents the correction of the image point coordinates in the left and right images, and it is obtained as follows:

$$\begin{cases} \Delta x = (x-x_0)(k_1r^2+k_2r^4) + (x-x_0) + p_2(r^2+2(x-x_0)^2) + 2p_1(x-x_0)(y-y_0) \\ \Delta y = (y-y_0)(k_1r^2+k_2r^4) + (y-y_0) + p_1(r^2+2(y-y_0)^2) + 2p_2(x-x_0)(y-y_0) \\ r = \sqrt{(x-x_0)^2+(y-y_0)^2} \end{cases} \tag{2}$$

where k_1 and k_2 are the first- and second-order radial distortion parameters, respectively; and p_1 and p_2 are the first- and second-order tangential distortion parameters, respectively.

During the camera calibration process, multiple sets of feature targets are uniformly distributed within the camera's field of view, thus meeting the coplanar condition. Therefore, using coplanar properties, a plane equation can be derived using the matched feature point coordinates and combined with the adjustment to improve the accuracy of the coordinate solution. Assuming that points $N_i(X_i, Y_i, Z_i)$, $N_1(X_1, Y_1, Z_1)$, $N_2(X_2, Y_2, Z_2)$, and $N_3(X_3, Y_3, Z_3)$ are on the same plane, the coplanar equation of the four points can be obtained as follows:

$$\begin{vmatrix} X_i - X_1 & Y_i - Y_1 & Z_i - Z_1 \\ X_i - X_2 & Y_i - Y_2 & Z_i - Z_2 \\ X_i - X_3 & Y_i - Y_3 & Z_i - Z_3 \end{vmatrix} = 0 \tag{3}$$

At the same time, a distance constraint can be constructed according to the location of the feature points, which can provide a reliable length reference for the adjustment model and ensure the accuracy of parameter calculation. If there are two feature points, the distance constraint of Eq. (4) can be constructed as follows:

$$\sqrt{(X_m - X_n)^2 + (Y_m - Y_n)^2 + (Z_m - Z_n)^2} - D_{mn} = \Delta D_{mn} \tag{4}$$

where (X_m, Y_m, Z_m) and (X_n, Y_n, Z_n) are the coordinates of the control points m and n in the photogrammetric coordinate system, respectively; D_{mn} is the high-precision laboratory-measured distance between the control points m and n; ΔD_{mn} is the residual between the distance obtained from the observation and the true distance of points m and n.

After linearization of Eq. (3) and Eq. (4), The final calibration model can be determined by combining collinear equations, feature point coplanarity, and distance constraints as follows[36]:

$$\begin{cases} \boldsymbol{V}_1 = \boldsymbol{A}\boldsymbol{t}_1 + \boldsymbol{C}\boldsymbol{X}_1 + \boldsymbol{F}_l\boldsymbol{X}_3 - \boldsymbol{L}_l\boldsymbol{P} \\ \boldsymbol{V}_2 = +\boldsymbol{B}\boldsymbol{t}_2 + \boldsymbol{D}\boldsymbol{X}_2 + \boldsymbol{F}_r\boldsymbol{X}_3 - \boldsymbol{L}_r\boldsymbol{P} \\ \boldsymbol{G}\boldsymbol{X}_4 - \boldsymbol{L}_1 = 0 \\ \boldsymbol{F}\boldsymbol{X}_5 - \boldsymbol{L}_2 = 0 \end{cases} \tag{5}$$

where $\boldsymbol{X}_4$ is the correction matrix of the 3D coordinates, $\boldsymbol{G}$ is the corresponding coefficient matrix, $\boldsymbol{L}_1$ is the corresponding residual matrix, $\boldsymbol{X}_5$ is the correction matrix of the virtual control point's coordinates, and $\boldsymbol{F}$ is the corresponding coefficient matrix; $\boldsymbol{L}_2$ is a constant term obtained by substituting the virtual control point's coordinates.

Then, Eq. (5) can be simplified as:

$$\begin{cases} \min \boldsymbol{V}^{\mathrm{T}}\boldsymbol{P}\boldsymbol{V} \\ \text{S.T.} \boldsymbol{V} = \boldsymbol{H}\boldsymbol{X} - \boldsymbol{L}\boldsymbol{P} \\ \boldsymbol{M}\boldsymbol{X} - \boldsymbol{N} = 0 \end{cases} \tag{6}$$

Using the Levenberg-Marquardt (LM) algorithm to optimize the parameter results, the normal equation corresponding to Eq. (6) can be established as follows [37]:

$$\begin{bmatrix} \boldsymbol{H}^T\boldsymbol{P}\boldsymbol{H} + \mu\boldsymbol{E} & \boldsymbol{H}^T\boldsymbol{M} \\ \boldsymbol{M}^T\boldsymbol{P}\boldsymbol{H} & \boldsymbol{M}^T\boldsymbol{P}\boldsymbol{M} \end{bmatrix} \begin{bmatrix} \boldsymbol{T} \\ \boldsymbol{X} \end{bmatrix} = \begin{bmatrix} \boldsymbol{H}^T\boldsymbol{P}\boldsymbol{L}_1 \\ \boldsymbol{M}^T\boldsymbol{P}\boldsymbol{L}_2 \end{bmatrix} \tag{7}$$

where μ is the damping coefficient; $\boldsymbol{H} = [\boldsymbol{A}, \boldsymbol{C}, \boldsymbol{F}_l, \boldsymbol{B}, \boldsymbol{D}, \boldsymbol{F}_r, \boldsymbol{0}, \boldsymbol{0}]$ and $\boldsymbol{M} = [\boldsymbol{0}, \boldsymbol{0}, \boldsymbol{0}, \boldsymbol{0}, \boldsymbol{0}, \boldsymbol{0}, \boldsymbol{G}, \boldsymbol{F}]$ are the coefficient matrices; $[\boldsymbol{T} \quad \boldsymbol{X}]$ is the camera calibration parameter vector to be obtained, and $[\boldsymbol{L}_1 \quad \boldsymbol{L}_2]$ is the residual vector.

According to the principle of least squares, the camera calibration parameters can be solved by:

$$\boldsymbol{X} = (\boldsymbol{N}_1^{-1} - \boldsymbol{N}_1^{-1}\boldsymbol{M}^T\boldsymbol{N}_2^{-1}\boldsymbol{M}\boldsymbol{N}_1^{-1})\boldsymbol{W} - \boldsymbol{N}_1^{-1}\boldsymbol{M}^T\boldsymbol{N}_2^{-1}\boldsymbol{N} \tag{8}$$

where $\boldsymbol{N}_1 = \boldsymbol{H}^T\boldsymbol{P}\boldsymbol{H}$, $\boldsymbol{N}_2 = \boldsymbol{M}\boldsymbol{N}_1^{-1}\boldsymbol{M}^T$, and $\boldsymbol{W} = \boldsymbol{H}^T\boldsymbol{P}\boldsymbol{L}$.

Then, the LM is used to optimize the solution to obtain the final calibration unit weight error and the measurement error of unknown parameters. The corresponding mathematical formula is as follows[38]:

$$\begin{cases} \sigma_0 = \sqrt{\dfrac{\boldsymbol{V}^{\mathrm{T}}\boldsymbol{P}\boldsymbol{V}}{n-r}} \\ \sigma_{xx} = \sigma_0\sqrt{\boldsymbol{Q}_{xx}} \end{cases} \tag{9}$$

where σ_0 is the unit weight root mean square error (RMSE); n is the number of observations used in the adjustment; r is the rank of the coefficient matrix of the unknown parameters; σ_{xx} indicates the median error of unknown calibration parameters, and $\boldsymbol{Q}_{xx} = \boldsymbol{N}_1^{-1} - \boldsymbol{N}_1^{-1}$

$\boldsymbol{M}^T\boldsymbol{N}_2^{-1}\boldsymbol{M}\boldsymbol{N}_1^{-1}$ is a hybrid matrix.

2.3. Cooperative feature target circle center fitting

The high-precision image point coordinates of feature points denote key data for 3D reconstruction. To analyze the motion state of a moving carrier effectively, this paper designs a target circle to extract the center image point coordinates, as shown in Fig. 3(a). First, the morphological operation is conducted to obtain the target circular pixel set, and the contour extraction is performed on the circular pixel set. As shown in Fig. 3(b), a pixel point on the upper left part of an object is selected as a starting point to start traversing; the direction is recorded, and its pixel value is set to zero. Then, the next boundary point is searched along the scanning direction following the tracking pixel consistency criterion. If there is a boundary point, the scanning direction rotates two grids counterclockwise; otherwise, the scanning direction rotates clockwise to complete the overall tracking and obtain complete contour information to complete the carrier boundary extraction. Finally, RANSAC method is used to establish the error function of Eq. (10) to screen the contour pixel set and fit the center of the circle to obtain accurate and reliable image point coordinates of the center of the target circle [31].

The specific steps are as follows. First, divide the contour data into correct and abnormal data and select sampling data from the source data randomly according to the occurrence probability of the correct data for initial center fitting and obtain the initial correct result. Then, substitute other data points into the initial fitting model and calculate the model accuracy score. Finally, sort the scores of all possible models to determine the most accurate and most reliable center-fitting model. The error function is derived as follows[39]:

$$(1-(1-e)^s)^N = 1-p \tag{10}$$

where e is the proportion of points outside the fitting buffer zone; s is the minimum number of model fitting solutions; p is the model fitting confidence; N is the number of model iterations.

Further, to improve the fitting accuracy of the center of the circle, after numerous experiments, in this study, the proportion of points outside the buffer zone e is set to 0.001, s is set to three, and the confidence level p is 0.99.

By using the above method, the image point coordinates with sub-pixel precision can be obtained, providing accurate and reliable basic data for the reconstruction of 3D coordinates of feature points.

2.4. Carrier motion state estimation by combining IMU and stereo vision

The 3D reconstruction of the characteristic target circle attached to a moving carrier is conducted by using the stereo measurement method, and the initial estimation of the moving state of the carrier is realized. Meanwhile, In order to mitigate the influence of the external forces on the measurement results of the carrier, the IMU is combined with stereo vision and used for state measurement.

The specific steps are as follows:

(1) Homography matrix calculation.

The homography matrix can describe the pose changes caused by factors such as rotation, translation, and affine transformation between carrier frames. If the homogeneous coordinates of the ith pair of matching points in the two frames of images before and after are $A_i = (x_i, y_i, 1)^T$ and $B_i = (x_i', y_i', 1)^T$, respectively; then, for the homography matrix $\boldsymbol{H}$, there is $\boldsymbol{B} = \boldsymbol{H}\boldsymbol{A}$, and it holds that[40]:

$$\begin{bmatrix} x_i' \\ y_i' \\ 1 \end{bmatrix} = \begin{bmatrix} h_{11} & h_{12} & h_{13} \\ h_{21} & h_{22} & h_{23} \\ h_{31} & h_{32} & h_{33} \end{bmatrix} \begin{bmatrix} x_i \\ y_i \\ 1 \end{bmatrix} \tag{11}$$

Further, to obtain reliable and accurate matrix parameters, multiple groups of points with the same name are used to construct the SVD to solve the matrix $\boldsymbol{H}$. First, based on the inter-frame images, the affine scale-invariant feature transform (Asift) is used to obtain the initial set of feature points with the same name, and n groups of points with the same name are selected to construct the homography matrix calculation equation as follows [41]:

$$\begin{cases} \boldsymbol{w}x = (x_1, y_1, 1, 0, 0, 0, -x_1x_1', -y_1x_1', -x_1') \\ \boldsymbol{w}y = (0, 0, 0, x_1, y_1, 1, -x_1y_1', -y_1y_1', -y_1') \end{cases} \tag{12}$$

$$\boldsymbol{W}\boldsymbol{H} = \boldsymbol{0} \tag{13}$$

where $\boldsymbol{H} = [h_{11}, h_{12}, h_{13}, h_{21}, h_{22}, h_{23}, h_{31}, h_{32}, h_{33}]^T$, and $\boldsymbol{W} = (\boldsymbol{w}x_1^T, \boldsymbol{w}y_1^T, \cdots, \boldsymbol{w}x_n^T, \boldsymbol{w}y_n^T)^T$.

When $n > 4$, the least squares normalization method and the SVD are combined for matrix decomposition to obtain the final homography matrix as follows[42]:

$$\begin{cases} \min\|\boldsymbol{W}\boldsymbol{H}\| \\ s.t.\|\boldsymbol{H}\| = 1 \\ \boldsymbol{W} = \boldsymbol{U}\boldsymbol{S}\boldsymbol{V}^T \end{cases} \tag{14}$$

Based on the singular value decomposition results, $S = diag(s_1, s_2, s_3)$, and $s_1 \gg s_2 \gg s_3$; according to the characteristics of scale equivalence, s_3 is set to zero, and $S' = diag((s_1+s_2)/2, (s_1+s_2)/2, 0)$; lastly, the final homography matrix is obtained by $\boldsymbol{H} = \boldsymbol{U}\boldsymbol{S}'\boldsymbol{V}^{\mathrm{T}}$.

(2) Dense matching of feature points.

Next, dense matching is performed on the initial homonymous points to obtain reliable motion parameters. First, a convex hull is drawn based on the feature points of the previous frame of a stereoscopic image, a Delaunay triangulation network is constructed, and a triangle index is obtained. Then, using the initial triangulation, the triangulation is encrypted according to the center of gravity criterion, and the accuracy of the encrypted homonymous triangulations with the same name is verified by combining epicenter constraints, feature constraints, and distance constraints [34] to obtain a robust and reliable encrypted homonymous points set.

As shown in Fig. 2, the homonymous points must be located on the corresponding epipolar line. Combining the coordinates of the image points with the same name and the principle of epipolar constraints, the epipolar line constraint equation is derived and denoted as an important criterion for the matching accuracy of the points with the same name [35,36]. Therefore, first, the RANSAC algorithm is used to estimate the fundamental matrix, and the *Sampson* distance from homonymous points to the model is calculated as a standard for measuring the internal and external points of the fundamental matrix model. The *Sampson* distance formula is calculated as follows[43]:

$$dis_{sampson}(x_i, y_i) = \left(y_i\boldsymbol{F}\boldsymbol{x}_i^T\right)^2 \left[\frac{1}{\left(\boldsymbol{F}\boldsymbol{x}_i^T\right)_1^2 + \left(\boldsymbol{F}\boldsymbol{x}_i^T\right)_2^2} + \frac{1}{\left(\boldsymbol{F}\boldsymbol{y}_i^T\right)_1^2 + \left(\boldsymbol{F}\boldsymbol{y}_i^T\right)_2^2}\right] \tag{15}$$

where (x_i, y_i) represents the pixel coordinates of the ith point with the same name in the left and right images; $\boldsymbol{F}$ is the estimated fundamental matrix; $\left(\boldsymbol{F}\boldsymbol{x}_i^T\right)_1^2$ represents the square of the first component vector of vector $\boldsymbol{F}\boldsymbol{x}_i^{\mathrm{T}}$, and $\left(\boldsymbol{F}\boldsymbol{y}_i^T\right)_1^2$ is the square of the second component vector of vector $\boldsymbol{F}\boldsymbol{y}_i^{\mathrm{T}}$.

Since the estimated rank of the matrix $\boldsymbol{F}$ differs from two due to noise interference, the SVD is used to solve it. In addition, a relative orientation linear transformation method, the relation orientation linear transformation (RLT), which is based on the coplanar condition, is used to determine the corresponding epipolar line. The epipolar line constraints can be constructed as follows[44]:

$$y_i' = \frac{(1-L_3^0)y_i - L_1^0 - L_2^0x_i - L_4^0x_i' - L_5^0x_ix_i' - L_7^0y_ix_i'}{1 + L_6^0x_i + L_8^0y_i} \tag{16}$$

where (x_i, y_i) and (x_i', y_i') are the coordinates of the reference image point and the target coordinates, respectively; L_j^0 is the coefficient

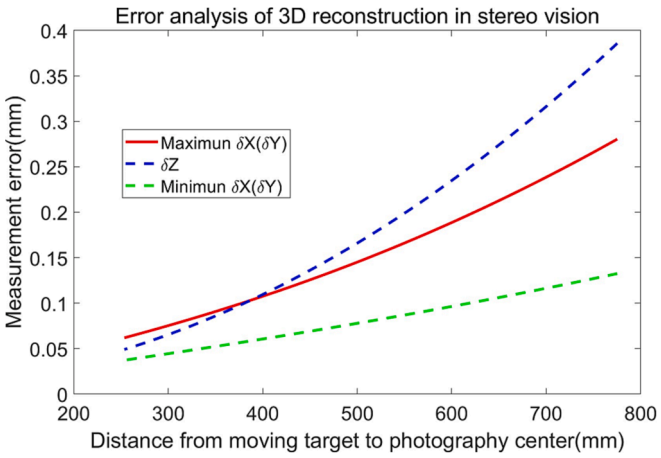

Fig. 4. The precision of the 3D coordinates of the checkpoints; the red line represents the maximum error curve in the × and *y* directions, the green dotted line is the minimum error curve in the × and *y* directions, and the blue dotted line is the error distribution curve in the *z* direction. The horizontal axis indicates the distance from the carrier to the photography center, expressed in mm, and the vertical axis represents the coordinate reconstruction error, also expressed in mm.

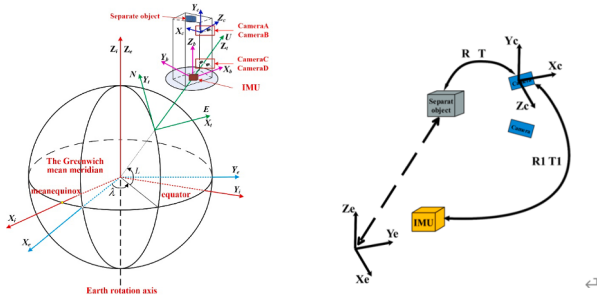

(a) Coordinate system (b) Measurement coordinate

Fig. 5. The carrier motion pose measurement coordinate system. In Fig. 5(a), the red coordinate axis denotes the geocentric inertial coordinate system, the blue coordinate axis is the Earth coordinate system, and the green coordinate axis is the geographic coordinate system; the pink coordinate axis is the carrier coordinate system, and the blue coordinate system is the camera coordinate system; the red matrix frame is the binocular stereo camera, and the brown object represents the IMU, which shows the latitude and longitude of the carrier in the Earth coordinate system. In Fig. 5(b), the coordinate transformation process for determining the final pose of the carrier is illustrated, and the specific steps are as follows. First, the coordinate system of the IMU relative to the Earth is determined. Then, the attitude matrix between the IMU and the stereo vision is obtained according to the installation position. Finally, the relationship between the stereo vision and the carrier is used to determine the coordinate system of the carrier relative to the Earth.

vector.

Based on the epipolar constraint, the Euclidean distance from the homonymous points on the right image to the epipolar is calculated and denoted as an initial accuracy screening condition. The zero-normalized cross-correlation (ZNCC) method is employed to improve the matching accuracy of the triangulation primitives with the same name, and the final triangulation set of the left and right images with the same name is constructed [37]. Meanwhile, the RANSAC is used to filter the accuracy of the matching results to ensure the matching accuracy of the homonymous points, and the final results of the homonymous points are obtained, which are recorded as ULp_{xy} and URp_{xy}.

(3) Inter-frame homonymous point conversion and 3D reconstruction.

Combining the homography matrices $\boldsymbol{H}_l$ and $\boldsymbol{H}_r$ between the left and right camera frames acquired by the initial feature points, the coordinates of the homonymous points corresponding to the encrypted feature points, DLp_{xy} and DRp_{xy}, are calculated as follows:

$$\begin{cases} DLp_{xy} = \boldsymbol{H}_l \cdot ULp_{xy} \\ DRp_{xy} = \boldsymbol{H}_r \cdot URp_{xy} \end{cases} \tag{17}$$

Based on the geometric relationship between the image points and the object space points in Fig. 2, the 3D coordinates of the feature points can be obtained using the coordinates of the image homonymous points. First, parallax d is calculated based on the abscissa values of the left and right image points with the same name. Then, following the principle of collinearity and combining the image point coordinates, baseline B, and focal length f, the depth of the feature point can be calculated. Finally, the 3D coordinates of the feature point can be solved as follows[45]:

$$d = x_l - x_r, X_p = \frac{B}{d}x_p = \frac{Y_p}{f}x_p, Y_p = \frac{B}{d}y_p = \frac{Y_p}{f}y_p, Z_p = \frac{B}{d}f \tag{18}$$

where $\left(x_p, y_p\right)$ represents the coordinates of the image point; B is the camera baseline; f is the focal length of the camera; d is the parallax corresponding to the homonymous points; (X_p, Y_p, Z_p) denotes the 3D coordinates corresponding to the feature point.

An accurate visual measurement scheme is the primary accuracy benchmark for carrier motion state measurement. Considering the influencing factors of the binocular stereo measurement, the 3D coordinate accuracy of the proposed method is analyzed. The coordinate error evaluation formula is as follows[46]:

$$\begin{cases} \sigma_X = \sqrt{\left(\frac{Z_p^2}{Bf}\right)^2\left(\frac{x}{f}\right)^2\sigma_d^2 + \left(\frac{Z_p}{f}\right)^2\sigma_x^2 + \left(\frac{x}{d}\right)^2\sigma_B^2 + \left(\frac{x}{f}\right)^2\left(\frac{B}{d}\right)^2\sigma_f^2} \\ \sigma_Y = \sqrt{\left(\frac{Z_p^2}{Bf}\right)^2\left(\frac{y}{f}\right)^2\sigma_d^2 + \left(\frac{Z_p}{f}\right)^2\sigma_y^2 + \left(\frac{x}{d}\right)^2\sigma_B^2 + \left(\frac{y}{f}\right)^2\left(\frac{B}{d}\right)^2\sigma_f^2} \\ \sigma_Z = \sqrt{\left(\frac{Z_p^2}{Bf}\right)^2\sigma_d^2 + \left(\frac{f}{d}\right)^2\sigma_B^2 + \left(\frac{y}{f}\right)^2\left(\frac{B}{d}\right)^2\sigma_f^2} \end{cases} \tag{19}$$

where $(\sigma_X, \sigma_Y, \sigma_Z)$ are the errors of plane and elevation coordinates; σ_d is the parallax accuracy; σ_B is the baseline measurement error; σ_f is the focal length calibration error.

Next, the camera calibration and center-fitting experiment are performed, and based on the actual measurement results, B is 270 mm, f is 2297 pixels, σ_x is 0.3 pixels, σ_d is 0.212 pixels, σ_B is 0.03 mm, and σ_f is 0.305 pixels. These values are used to obtain the reconstruction accuracy statistics, which are shown in Fig. 4.

As shown in Fig. 4, when the carrier is 0.4 m away from the photography center, the reconstruction accuracy of the proposed method is approximately 0.1306 mm, which is about 0.727 pixels and can ensure the measurement accuracy of the carrier pos. Therefore, based on the coordinates of the homonymous points in the front and rear frames and the calibration parameters of the left and right cameras, the 3D coordinate set of the front frame $UX_wY_wZ_w$, the 3D coordinate set of the rear frame $DX_wY_wZ_w$, and rear frames corresponding to the homonymous points between frames can be obtained by the triangulation method.

(4) Carrier pose measurement.

By combining the 3D coordinates of the homonymous points in the inter-frame image of the carrier and the similarity transformation model, the pose change of the carrier can be determined [38]. The similarity transformation relationship is given as follows[47]:

$$\begin{bmatrix} x_{1i} \\ y_{1i} \\ z_{1i} \end{bmatrix} - \begin{bmatrix} ex_{1i} \\ ey_{1i} \\ ez_{1i} \end{bmatrix} = \lambda \boldsymbol{R}\left(\begin{bmatrix} x_{2i} \\ y_{2i} \\ z_{2i} \end{bmatrix} - \begin{bmatrix} ex_{2i} \\ ey_{2i} \\ ez_{2i} \end{bmatrix}\right) + \begin{bmatrix} \Delta X \\ \Delta Y \\ \Delta Z \end{bmatrix} \tag{20}$$

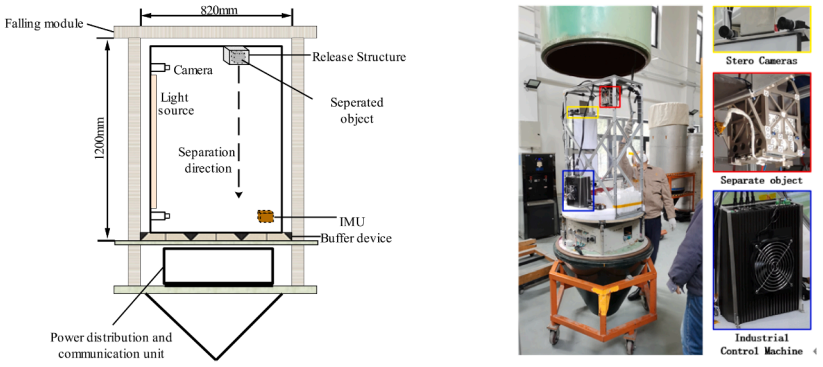

(a) Drop cabin internal design structure (b) Measuring equipment composition diagram

Fig. 6. The schematic diagram of the motion state measurement platform: (a) the cross-sectional view of the installation of the internal platform of the drop cabin, including the motion measurement platform and power distribution and communication units; (b) the actual installation diagram of the measurement equipment, where the yellow rectangle denotes the stereo measurement camera, the red rectangle is the release structure with the carrier, and the blue rectangle represents the industrial computer that controls imaging and image storage.

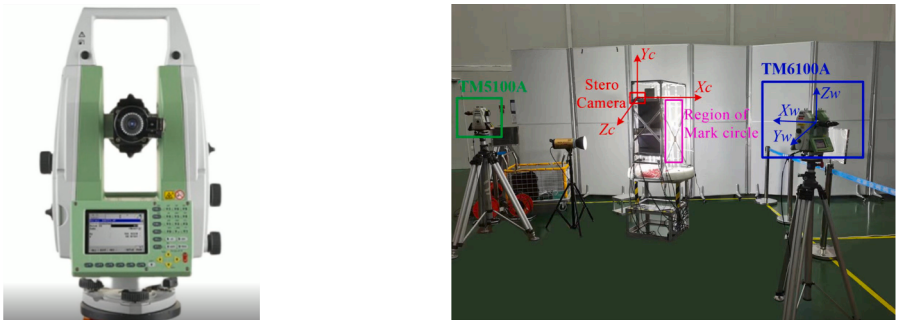

(a) TM6100A Theodolite (b) The scene of the calibration experiment

Fig. 7. (a). The TM6100A high-precision theodolite measurement system; the photo of the Leica TM6100A was taken from the official Leica product manual; (b) the camera calibration control field, where the green and blue rectangles relate to the TM5100A and TM6100A, respectively; the red matrix indicates the stereo camera, and the pink area represents the target point area.

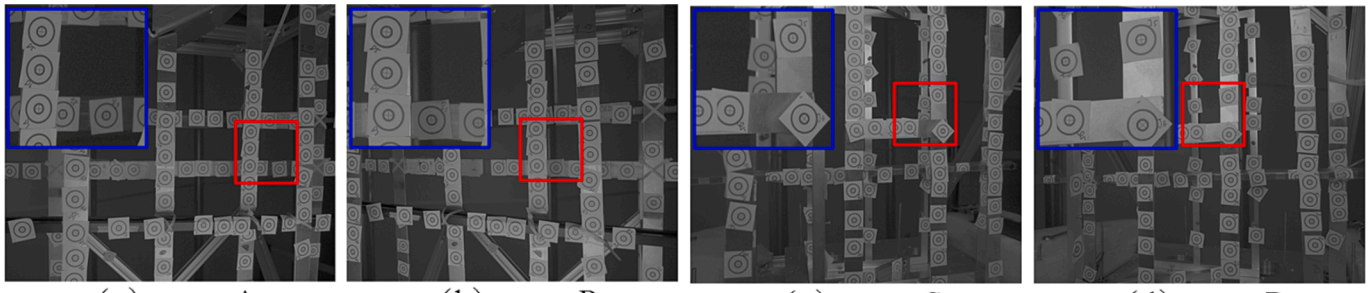

Fig. 8. (a)–(d) The stereo images taken by the two sets of stereo cameras; the red rectangle is the characteristic target circle, and the blue sub-image in the upper left corner denotes the enlarged image of the red area.

$$\boldsymbol{R} = \boldsymbol{R}_{\varphi}\boldsymbol{R}_{w}\boldsymbol{R}_{k} = \begin{bmatrix} \cos\varphi & 0 & -\sin\varphi \\ 0 & 1 & 0 \\ \sin\varphi & 0 & \cos\varphi \end{bmatrix} \begin{bmatrix} 1 & 0 & 0 \\ 0 & \cos w & -\sin w \\ 0 & \sin w & \cos w \end{bmatrix} \begin{bmatrix} \cos k & -\sin k & 0 \\ \sin k & \cos k & 0 \\ 0 & 0 & 1 \end{bmatrix} \tag{21}$$

where $[x_{1i}, y_{1i}, z_{1i}]^T$ and $[x_{2i}, y_{2i}, z_{2i}]^T$ are the 3D coordinates of the feature points of the front and back frames, respectively; $[ex_{1i}, ey_{1i}, ez_{1i}]^T$ and $[ex_{2i}, ey_{2i}, ez_{2i}]^T$ are the 3D coordinate errors of the feature points of the front and back frames, respectively; λ is the similar change scale parameter; $\varphi - w - k$ is the rotation angle of the two coordinate systems around $Y - X - Z$ direction; $\boldsymbol{R}$ is the rotation matrix constructed by the pose angle; $[\Delta X, \Delta Y, \Delta Z]^T$ is the offset of the origin of the virtual coordinate system of the two frames of images.

By performing the overall least squares adjustment, the error of the origin offset and pose angle ($\delta\widehat{\varepsilon}$) can be obtained as follows[48]:

$$\delta\widehat{\varepsilon} = \left(\boldsymbol{A}^T\boldsymbol{Q}_{ll}^{-1}\boldsymbol{A}\right)^{-1}\boldsymbol{A}^T\boldsymbol{Q}_{ll}^{-1}\boldsymbol{L} \tag{22}$$

where $\boldsymbol{A}$ is the pose change parameter coefficient matrix, $\boldsymbol{Q}_{ll}$ represents the correlation factor matrix, and L is the 3D coordinate residual vector.

(5) Absolute pose determination by Combining IMU and Stereo Vision.

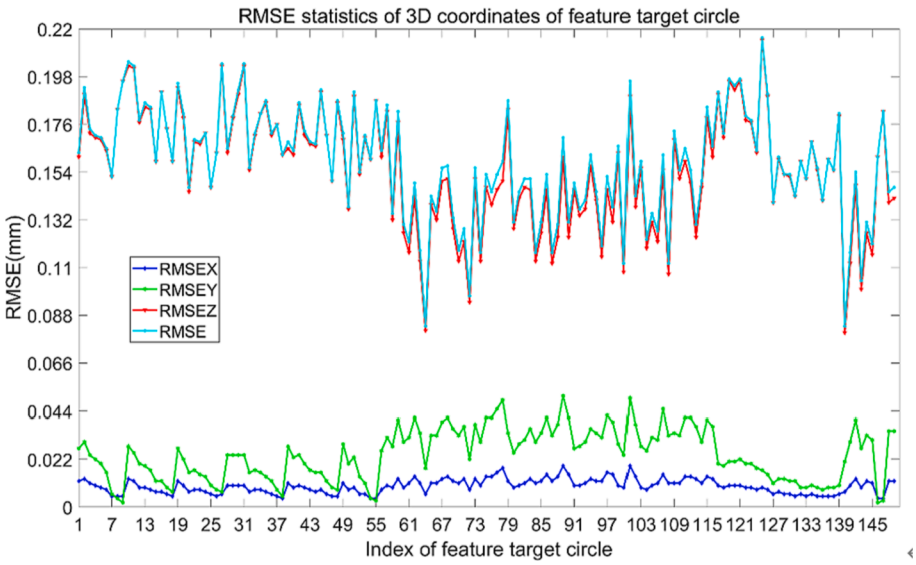

Fig. 9. Accuracy statistics of the control points. The horizontal axis shows the index of the characteristic circle target, and the vertical axis represents the RMSE value expressed in mm; the blue, green, red, and cyan marked broken lines denote the X,Y, and Z and comprehensive RMSE error values, respectively.

Table 1
The calibration results and RMSE of the IO.

IO and RMSE	f_x (pixel)	f_y (pixel)	x_o (pixel)	y_o (pixel)	k_1	k_2	p_1	p_2
IO of CameraA	2297.142	2297.096	11.953	−39.634	−1.130E-08	1.519E-15	2.492E-07	−1.270E-07
RMSE of CameraA	1.066	1.108	1.408	1.072	4.15E-10	1.86E-16	9.02E-08	7.62E-08
IO of CameraB	2309.058	2308.147	−7.848	−15.872	−1.284E-08	2.225E-15	5.219E-07	1.818E-07
RMSE of CameraB	1.626	1.506	1.738	1.214	4.693E-10	2.136E-16	1.168E-07	8.232E-08
IO of CameraC	2310.347	2310.185	30.263	−28.563	−1.280E-08	1.916E-15	5.707E-07	−7.537E-09
RMSE of CameraC	2.277	2.26	3.31	2.46	8.10E-10	3.32E-16	1.90E-07	1.53E-07
IO of CameraD	2305.337	2304.977	36.234	−38.596	−1.238E-08	2.088E-15	−2.304E-07	1.071E-07
RMSE of CameraD	1.58	1.66	1.656	1.317	4.59E-10	2.44E-16	9.63E-08	9.05E-08

Table 2
The calibration results and RMSE of the EO.

EO and RMSE	X_S (mm)	Y_S (mm)	Z_S (mm)	φ(rad)	w(rad)	k(rad)
EO of CameraA	−2071.620	253.539	−1047.431	0.141	−0.028	0.001
RMSE of CameraA	0.047	0.044	0.137	5.94E-4	4.81E-4	4.83E-5
EO of CameraB	−1840.599	251.762	−1067.373	−0.374	−0.017	−0.020
RMSE of CameraB	0.137	0.057	0.152	7.84E-4	5.20E-4	6.43E-5
EO of CameraC	−2080.046	−469.929	−1046.695	0.138	−0.005	−0.006
RMSE of CameraC	0.098	0.063	0.378	1.30E-4	9.81E-4	1.02E-4
EO of CameraD	−1848.488	−472.939	−1064.793	−0.366	0.015	−0.018
RMSE of CameraD	0.100	0.061	0.243	6.80E-4	5.99E-4	6.01E-5

Table 3
The errors of different methods for 30 checkpoints.

Method	Error (mm)		
	Average	Max	RMSE
Proposed method	0.0348	0.1157	0.0706
Self-calibration bundle adjustment	0.0623	0.1423	0.1035
CAHVOR [52]	0.092	0.182	0.1124
Vanishing points [53]	0.1063	0.2014	0.1225

The absolute pose change of the carrier relative to the center of the Earth is determined according to the spatial relationship between the carrier, the stereo camera, and the IMU [49]. The coordinate system constructed by fusing the IMU and stereo cameras is presented in Fig. 5 (a).Fig. 6..

According to the characteristics of data collected by the IMU, it can be known that the coordinate conversion matrix from the carrier coordinate system b to the navigation coordinate system t is given by[50]:

$$\boldsymbol{R}_b^t = \begin{bmatrix} cos\psi cos\gamma - sin\psi sin\theta sin\gamma & -sin\psi cos\theta & cos\psi sin\gamma + sin\psi sin\theta cos\gamma \\ cos\psi sin\theta sin\gamma + sin\psi cos\gamma & cos\theta cos\psi & sin\psi sin\gamma - cos\psi sin\theta cos\gamma \\ -cos\theta sin\gamma & sin\theta & cos\theta cos\gamma \end{bmatrix} \tag{23}$$

where ψ, θ and γ are the heading angle around the Z-axis, the pitch angle around the X-axis, and the roll angle around the Y-axis, respectively.

Further, combined with the conversion relationship between the Earth coordinate system, the Earth-centered inertial coordinate system, and the navigation coordinate system, the transformation matrix from the carrier coordinate system to the Earth-center coordinate system can be determined as follows:

$$\boldsymbol{R}_b^i = \boldsymbol{R}_e^i \boldsymbol{R}_t^e \boldsymbol{R}_b^t \tag{24}$$

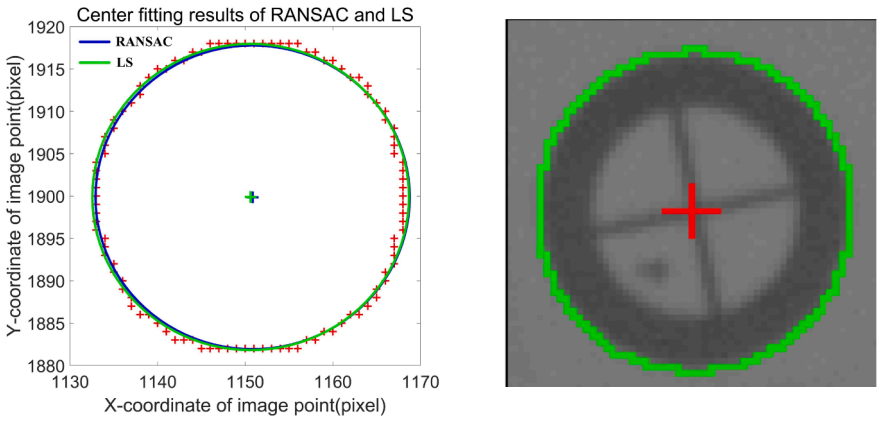

(a) Center-fitting comparison results (b) RANSAC fitting results

Fig. 10. (a) The fitting results of the two methods; the red '+' is the pixel on the circle, and the blue and green circles denote the results of the RANSAC and LS fitting methods, respectively; (b) the final fitting effect.

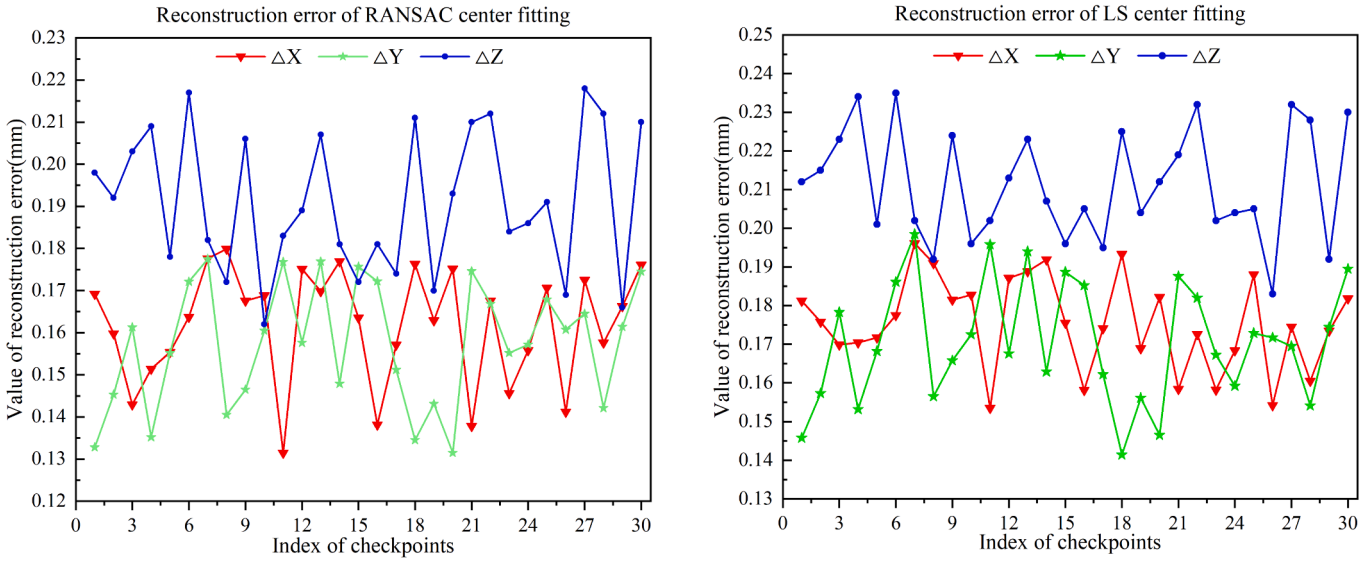

(a) 3D reconstruction error of the RANSAC (b) 3D reconstruction error of the LS

Fig. 11. The 3D reconstruction error results of the two fitting methods; in (a) and (b), the horizontal axis denotes the index of the checkpoint, and the vertical axis represents the coordinate deviation, expressed in mm. The red, green, and blue fold lines are the coordinate deviation statistical curves of the inspection points in the X,Y, and Z directions, respectively.

Table 4
The coordinate deviation results of checkpoint reconstruction performed by the RANSAC and LS fitting methods.

Deviation indicator	RANSAC			LS		
	$\triangle x$ (mm)	$\triangle y$ (mm)	$\triangle z$ (mm)	$\triangle x$ (mm)	$\triangle y$ (mm)	$\triangle z$ (mm)
Average	0.162	0.157	0.191	0.175	0.170	0.211
Min	0.132	0.133	0.162	0.154	0.141	0.183
Max	0.180	0.178	0.218	0.196	0.199	0.235

where $\boldsymbol{R}_t^e$ and $\boldsymbol{R}_e^i$ are transformation matrices from the navigation coordinate system to the Earth coordinate system and from the Earth coordinate system to the Earth-centered inertial coordinate system, respectively.

Next, based on the above IMU and stereo vision measurement results, the motion state parameters of the carrier in the geocentric coordinate system can be determined, and the specific steps are as follows:

(a) According to the circular coordinates of the target captured by the camera and the 3D coordinates of the feature points in the inertial navigation coordinate system, the pose matrix $\boldsymbol{R}_c^{in}$ between the camera and the IMU can be obtained by:

$$\begin{bmatrix} X_{in} \\ Y_{in} \\ Z_{in} \end{bmatrix} = \boldsymbol{R}_c^{in} \begin{bmatrix} X_C \\ Y_C \\ Z_C \end{bmatrix} \tag{25}$$

(b) After fixing the installation position of the IMU, by combining $\boldsymbol{R}_e^i$ and the inertial navigation pose data, the pose matrix $\boldsymbol{R}_c^{in}$ between the inertial navigation and the camera in the working state can be determined by:

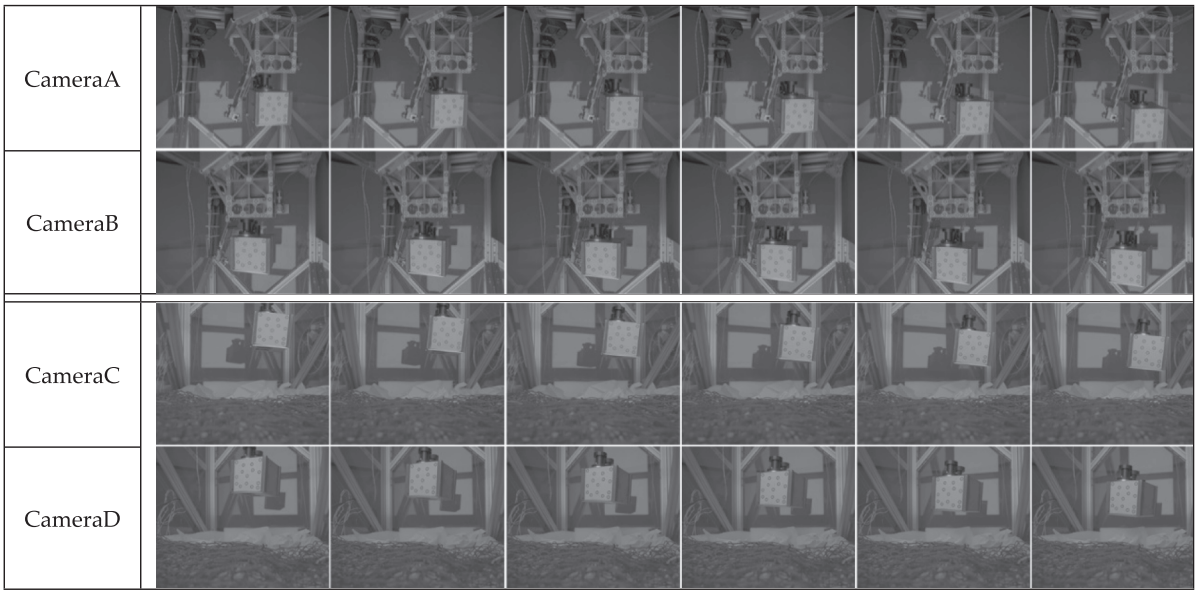

Fig. 12. The motion carrier landing sequence images obtained by the four cameras.

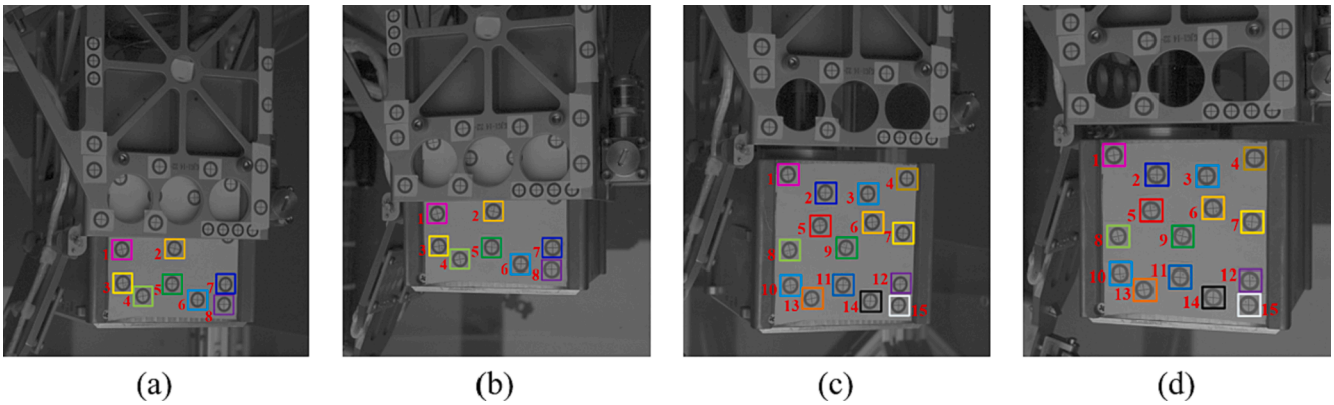

Fig. 13. (a), (b) Homonymous points selected inside the release structure; (c), (d) homonymous points selected by the carrier in the release stage of the release structure; squares of different colors denote pairs of the homonymous points; red numbers represent the number of feature points.

$$\boldsymbol{R}_c^{in} = \boldsymbol{R}_{in}^{iT}\boldsymbol{R}_c^i \tag{26}$$

(c) The stereo camera shoots the carrier, and the pose matrix of the carrier $\boldsymbol{R}_f^i$ in the inertial coordinate system at each moment can be determined using $\boldsymbol{R}_f^c$, $\boldsymbol{R}_c^{in}$ and $\boldsymbol{R}_{in}^i$ as follows:

$$\boldsymbol{R}_f^i = \boldsymbol{R}_{in}^i\boldsymbol{R}_c^{in}\boldsymbol{R}_f^c \tag{27}$$

(d) According to the components of $\boldsymbol{R}_f^i$, the pose matrix can be decomposed to obtain the rotation angle information on each axis, which can be combined with the time data to determine the angular velocity index of the carrier. The corresponding mathematical expressions are as follows[51]:

$$\begin{cases} \varphi = arctan\left(-\dfrac{\boldsymbol{R}_{f13}^i}{\boldsymbol{R}_{f33}^i}\right) \\ \varpi = arcsin\left(-\boldsymbol{R}_{f23}^i\right) \\ k = arctan\left(\dfrac{\boldsymbol{R}_{f21}^i}{\boldsymbol{R}_{f22}^i}\right) \end{cases} \tag{28}$$

where φ, ϖ and k are the rotation angles of the object around the Y, X, and Z axes in the camera coordinate system, respectively.

The actual three-dimensional measurement data between different frames are used to verify the accuracy of the pose angle; the error of the pose angle is better than 0.09°, and angular velocity accuracy is 0.127°/s.

3. Experimental results analysis

In the field of planetary science, precise measurement of the motion state of a moving carrier represents an important part of scientific exploration missions. Considering the problem that the ground environment cannot meet the microgravity conditions in deep space and can cause measurement errors, this study constructs a motion carrier state estimation and measurement platform. A microgravity environment was constructed using the drop tower of the Institute of Mechanics, Chinese Academy of Sciences. The drop tower included the release device, drop cabin, and recovery device, and the overall drop height was approximately 116 m. The release device controlled the drop cabin to achieve free fall, and the recovery device ensured the safe landing of the drop cabin. The internal space of the drop cabin could reach a microgravity environment, the effective microgravity time was roughly 3.25 s, and the microgravity level was $10^{-2}g$.

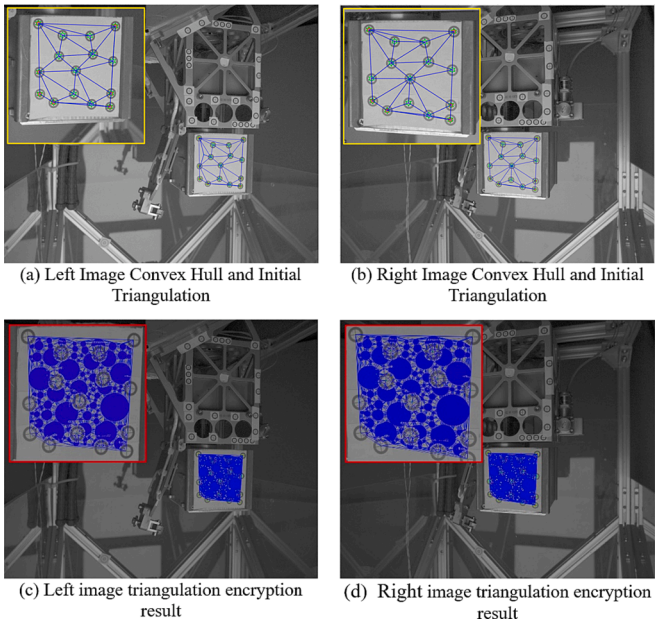

(a) Left Image Convex Hull and Initial Triangulation

(b) Right Image Convex Hull and Initial Triangulation

(c) Left image triangulation encryption result

(d) Right image triangulation encryption result

Fig. 14. The diagram of the triangular network encryption process on the surface of the carrier: (a), (b) the initial convex hull and the triangular network of the left and right images, respectively; (c), (d) the encryption effects of the feature points of homonymous points; the green diamond points denote the initial homonymous points, and the blue points are the encrypted homonymous points; the red area on the left represents the enlarged image of the TIN construction.

Table 5
The results of the inter-frame homography matrix of a stereo camera.

Category	Homography matrix between frames 154 and 155
H_l	1.004655 0.013263 - 15.381336 - 0.006016 1.0133807 34.146829 - 1.783383e - 06 7.484501e - 06 1
H_r	0.993209 0.007598 0.017758 0.000485 1.007429 25.730181 - 3.846882e - 06 5.004364e - 06 1

3.1. Carrier motion state measurement platform

To measure the pose change of the carrier in a microgravity environment accurately and verify the control performance of the release structure, a carrier motion state measurement platform was constructed. The platform included a protective bracket, a binocular stereo camera, an IMU, a light source, an industrial computer, and a release structure. The protective bracket was used as a platform foundation for the above-mentioned equipment. The binocular stereo camera and IMU were used for image acquisition during the movement of the carrier and the data measurement of the landing pose. The light source provided light illumination during the landing. The industrial computer was used for data storage, and the release structure controlled the carrier release.

The main process of the carrier state measurement was as follows. First, the measuring platform equipment was fixed on the drop-off disc and sealed up. Then, the drop cabin was connected with the drop tower release device, and the height was increased to be landed. Finally, the release device was controlled at the ground station to release the drop cabin, enter the microgravity environment, and use the PLC to control the release of the carrier inside the release structure. Further, two sets of stereo cameras and IMU were controlled to complete synchronous imaging of the carrier landing process, which provided basic data for motion state parameter estimation.

3.2. Measurement coordinate system establishment and camera calibration

Aiming to obtain accurate camera parameters, this study calibrated two sets of stereo cameras using the control field calibration method, and characteristic targets were arranged in the field of view of the stereo cameras as control points. First, the high-precision theodolite TM5100A and TM6100A with an angle measurement accuracy of 0.5″ and a reference ruler were used to measure the 3D coordinates of the feature points in the target circle area in the experimental field. Moreover, the world coordinate system was defined, as presented by the blue coordinate system in Fig. 7(b). Then, the camera coordinate system was constructed according to the installation positions of the two sets of stereo cameras, which is denoted by the red coordinate system in Fig. 7(b), where the Y-axis is + clockwise, and the X and Z axes are + counterclockwise. The method presented in Section 2.3, the cooperative feature target circle center-fitting method, was used to extract the coordinates of the center image point of the target. Based on the measurement results and the geometric relationship between the feature points, the camera calibration method with additional geometric constraints was employed to calculate camera parameters.

A total of 149 characteristic circular targets were arranged in the field of view of the two sets of stereo cameras; cameras A and B had 62 and 55 effective calibration control points, respectively, and cameras C and D had 48 effective calibration control points, as shown in Fig. 8. The 3D coordinates of all target points were measured by the intersection of theodolite, and the coordinates in the X,Y, and Z directions were obtained, as well as the overall coordinate RMSE. The statistical results are shown in Fig. 9.

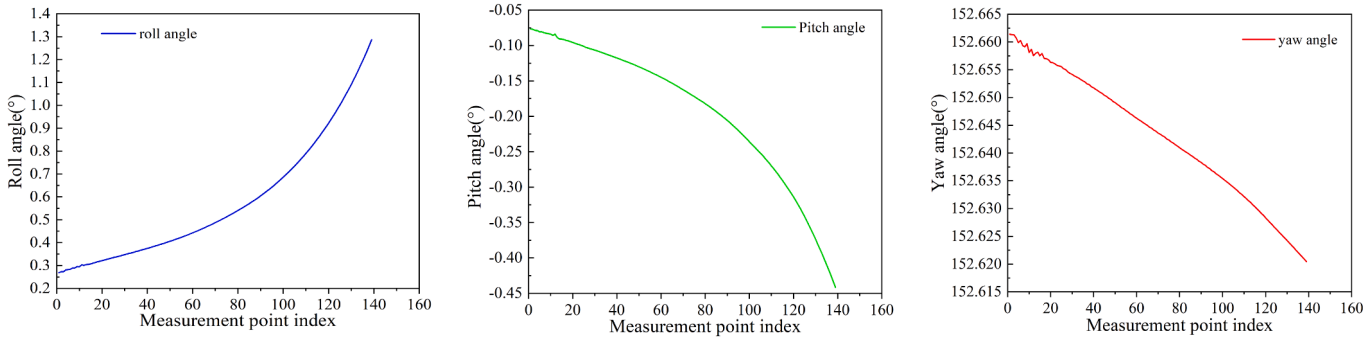

(a) Roll angle (b) Pitch angle (c) Yaw angle

Fig. 15. (a)–(c) The roll, pitch, and yaw angles measured by the IMU during the carrier landing process; the horizontal axis shows the sampling point index, and the vertical axis indicates the measured angle.

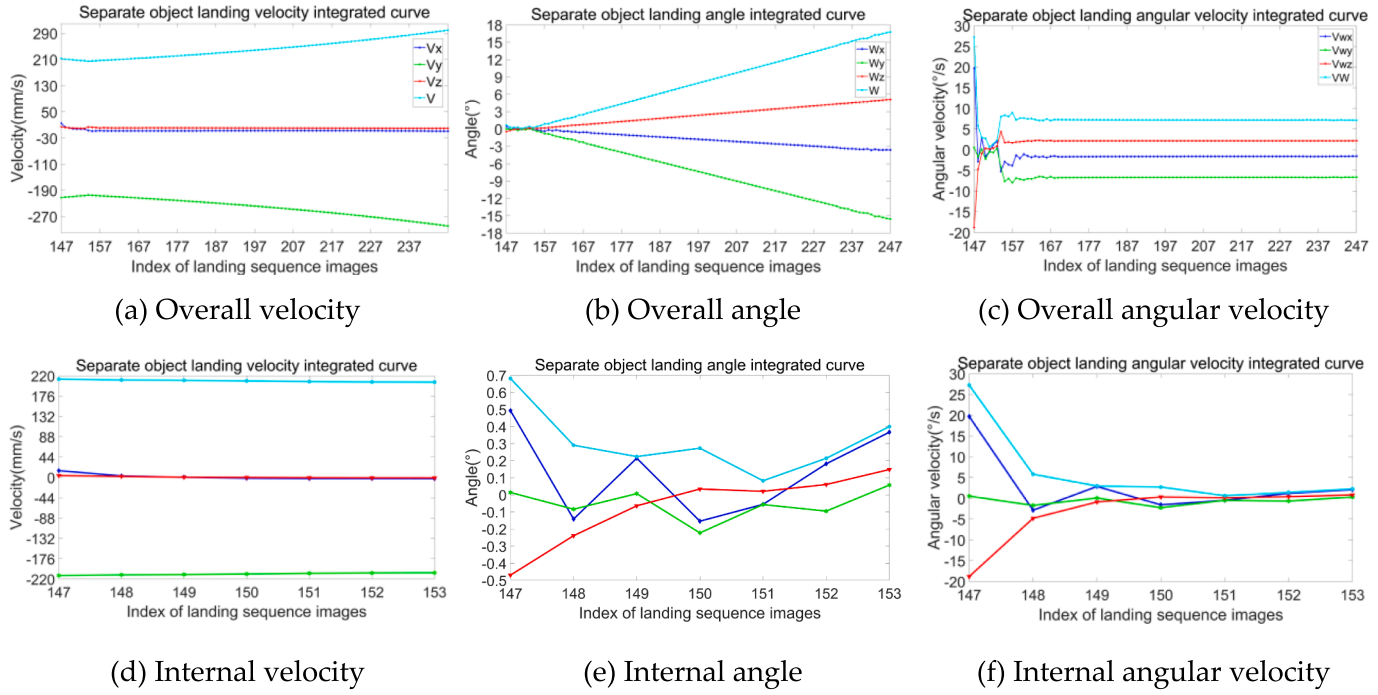

Fig. 16. (a)–(c) The overall initial reference data of the running velocity, angle, and angular velocity curves of the carrier, respectively; (d)–(f) the velocity, angle, and angular velocity movement curves of the carrier inside the release structure, respectively.

The statistical results in Fig. 9 show that the average values of the 149 control points in the three directions and the comprehensive RMSE were 0.0096 mm, 0.0242 mm, 0.1559 mm, and 0.1586 mm, and their maximum values were 0.019 mm, 0.051 mm, 0.215 mm, and 0.216 mm, respectively. Therefore, high-precision control point data could be obtained for the overall measurement system. Based on the above-presented data, by using the camera calibration method presented in Section 2.2 to conduct a joint calibration experiment on two sets of stereo cameras, the internal parameters (interior orientation elements—IO) and external parameters (exterior orientation elements—EO), distortion parameters, the corresponding root mean square error values were calculated, as shown in Tables 1 and 2.

In Tables 1 and 2, the IO and EO parameters of the cameras obtained by the proposed calibration method are presented. After calculation, the errors of the calibration unit weights of the four cameras were 0.305 pixels, 0.324 pixels, 0.379 pixels, and 0.255 pixels. These results indicated that the proposed method could achieve high-precision calibration parameters, thus providing a benchmark for the 3D high-precision reconstruction of feature points. In addition, to verify the reliability of the proposed calibration method, 30 checkpoints on the release structure were selected for accuracy verification, and the theodolite intersection measurement data were used as the ground-truth data. The results of the methods were compared with the coordinates obtained by the total station measurement system. Table 3 shows the error results at 30 checkpoints obtained by different methods.

The statistical results of the coordinate deviation of the inspection points in Table 3 show that the 3D coordinate deviation of the calibration parameters was the smallest for the proposed method, having an average measurement error of 0.0348 mm. Further, to verify the accuracy of the calibration results, the proposed method was compared with the classic self-calibration bundle adjustment method, the CAHVOR, and vanishing points [54]. The results indicated that the average measurement error of the proposed method was reduced by 44.14%, 62.17%, and 67.26%, while the RMSE was reduced by 31.79%, 37.19%, and 42.37%, respectively. The verification results fully demonstrate the reliability and effectiveness of the proposed calibration method.

3.3. Center fitting of circular target

An accurate extraction of feature point image point coordinates is crucial for 3D reconstruction. The method presented in Section 2.3 was used to fit the center of the pixels on the contour circle to obtain the final image point coordinates. To realize the model fitting, the least squares method has been commonly used to estimate the unknown parameters in the known law or model hypothesis empirical formula. It should be noted that when the amount of fitting data is large and the accuracy is relatively stable, the model fitting effect of this method is good, and a reliable fitting model can be obtained [55]. However, in practical applications, there are usually extreme points in the data point set, which could lead to deviations in the predicted value and cause the model fitting algorithm to fall into a local optimum, thereby reducing the fitting accuracy. This problem can be addressed by using the RANSAC method, which is a simple parameter estimation method based on data points and has good robustness. Therefore, this method was selected in this study to estimate reliable parameters from noisy data sets.

Further, to improve the visualization effect of the model fitting of the two methods, the least squares (LS) fitting method and the RANSAC method, a comparison experiment of circle center fitting was conducted. The center-fitting results of the two methods are shown in Fig. 10(a); Fig. 10(b) shows the final center-fitting result of the circular target.

The visualization effect of the center fitting indicated that the fitting circle obtained by the RANSAC method had a higher degree of fitting to the actual pixel than that obtained by the LS fitting method. Meanwhile, the fitting accuracy and robustness of the two methods were evaluated by the indirect method. Based on the global coordinate system, 30 inspection points were selected, and the 3D coordinate reconstruction was completed by using the center-fitting results of the RANSAC and LS fitting methods. The results were compared with the ground truth of the 3D coordinates measured by the theodolite and a standard ruler. The fitting accuracy of the two methods was tested by calculating the coordinate deviation in the three-axis direction. The statistical chart of the coordinate deviations of the inspection point and the quantitative statistical results of the deviation are presented in Fig. 11 and Table 4, respectively.

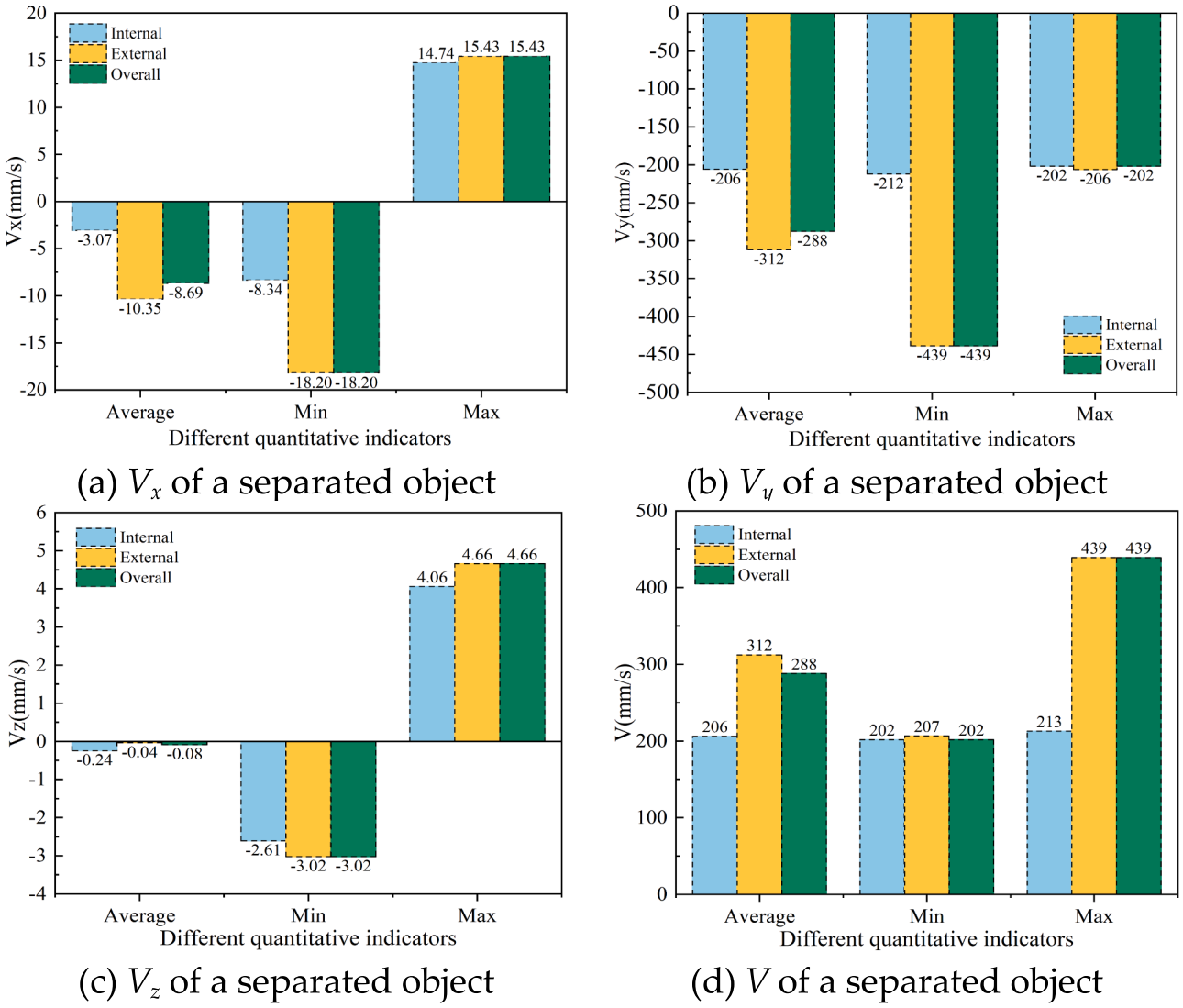

Fig. 17. The statistics of the velocity index of the carrier at different stages: (a)–(c) the velocity components in the X,Y, and Z directions, respectively; (d) the comprehensive velocity. The horizontal axis indicates the average, minimum, and maximum values of the falling velocity of the carrier in different intervals, and the vertical axis represents the velocity.

Based on the statistical results of the 3D coordinate deviations of the inspection point, the maximum reconstruction deviations in the X,Y, and Z directions were 0.016 mm, 0.021 mm, and 0.017 mm, while the minimum reconstruction deviations were 0.022 mm, 0.008 mm, and 0.021 mm. respectively. This indicates that the RANSAC method had higher accuracy of 3D coordinate reconstruction in obtaining the center image point than the LS method. Meanwhile, the average deviation of the former in the X,Y, and Z directions was increased by 7.75%, 7.66%, and 9.54%, respectively, compared to the latter, thus indicating that the center-fitting method based on the RANSAC was more robust and more stable.

3.4. Carrier motion state measurement results

Based on the above-presented experimental results, the carrier state measurement experiment was conducted. After the cabin entered a microgravity environment, two sets of stereo cameras were triggered to take pictures synchronously, and a total of 340 frames of the original images were obtained. The fields of view of cameras A and B contained a total of 32 images with an image index of 137–168, and those of cameras C and D contained a total of 15 images with an image index of 233–247. The specific details of the landing sequence images are shown in Fig. 12.

(1) Initial feature homonym point extraction.

To obtain stable and reliable motion state parameters and evaluate the performance of the trigger device of the release structure comprehensively, the landing process of the carrier was divided into two stages of motion; in one of them, the carrier was inside the release structure, and in another, the carrier was completely separated from the release structure; the carrier motion state for the two stages was estimated separately. Therefore, based on the motion sequence images, eight and 15 pairs of the initial feature points with the same name were selected for the internal and external states of the release structure, respectively, as shown in Fig. 13.

(2) Encryption of points with the same name and solution to the inter-frame homography matrix.

Next, to improve the reliability of the motion state parameter estimation, the initial feature points were densely matched using the method presented in Section 2.4, and the 3D coordinates of encrypted feature points were obtained to calculate the motion state parameters. The matching results of the homonymous triangulations encrypted feature points are shown in Fig. 14.

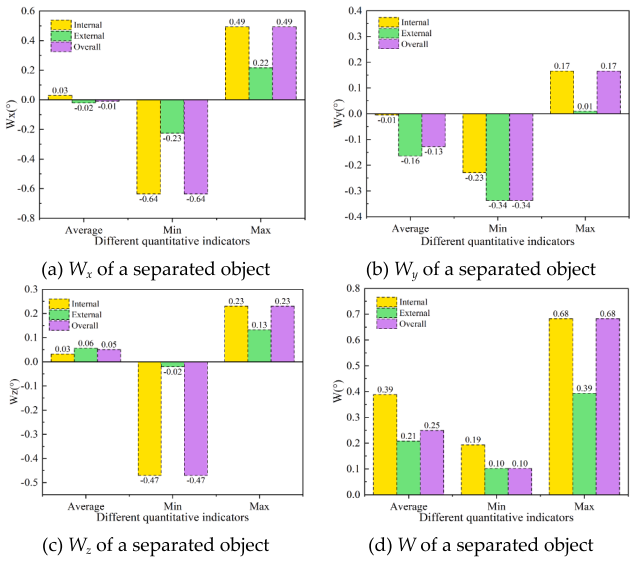

(a) W_x of a separated object (b) W_y of a separated object

(c) W_z of a separated object (d) W of a separated object

Fig. 18. The statistics of the angle index of the carrier at different stages: (a)–(c) the angle components in the X,Y, and Z directions, respectively; (d) the comprehensive angle. The horizontal axis shows the average, minimum, and maximum values of the falling angle of the carrier in different intervals, and the vertical axis represents the changing angle of the carrier along the three directions.

Furthermore, the initial inter-frame homography matrix was used to solve the inter-frame homonymous coordinates of encrypted points to ensure that the landing sequence images had homonymous points. The results of the homography matrix between the 154th and 155th frames in the left and right images are presented in Table 5.

(3) Carrier state parameter estimation.

The IMU and the stereo vision method were integrated to perform the precise measurement of the carrier's state parameters. First, the IMU and stereo vision system were used for data collection before landing; namely, the IMU measured the pose changes during the landing process, and the stereo vision measured the movement pose of the carrier. Then, according to the sampling rate of the IMU and stereo camera, the two sets of data were time-aligned by the interpolation method to ensure the unity of measurement data. Finally, the method introduced in Section 2.5 was employed to estimate the motion state parameters of the carrier. The change curves of the roll, pitch, and yaw angles of the IMU obtained through statistics are shown in Fig. 15.

According to the pose angle value obtained in the IMU test, the pose data of the measurement platform at the corresponding moment could be obtained. Combined with the relative pose data of the IMU and camera and the pose data of the carrier in the camera coordinate system, the pose change of the carrier relative to the center of the Earth was obtained. Then, the absolute pose change of the carrier was determined, thus avoiding the interference of the external forces. In addition, to analyze the motion state of the carrier and the performance of the release structure device accurately, based on the initial image, the statistical analysis of the motion parameters of the separation carrier (e.g., the velocity, angle, and angular velocity) in the internal, external, and overall stages of the release structure was conducted. The analysis results are shown in Fig. 16.

The measurement results indicated that the velocity of the carrier along the X-axis direction during the movement was from 14.74 mm/s at the beginning to −2.4471 mm/s after it was completely separated, showing a downward trend. Meanwhile, the velocity along the Y-axis direction V_y was the largest. When the detached camera started to fall, the velocity was approximately 212 mm/s. After it was completely detached, the velocity was 206.289 mm/s and remained relatively stable. The velocity along the Z-axis direction was the smallest, and the maximum V_z was 4.06 mm/s. The velocity after the carrier was completely separated from the release structure was −0.797 mm/s, and there was basically no change in the velocity. During the falling process of completely breaking away from the release structure, the velocity of the carrier along each axis tended to increase. The velocities in the three directions before falling were −9.173 mm/s, −299.0058 mm/s, and −0.6090 mm/s, which showed that the carrier had certain acceleration during the landing process, indicating that the experimental environment might not fully meet the microgravity environment standard.

At the same time, according to the angle and angular velocity motion curves of the carrier, the carrier rotated irregularly inside the release structure due to the elastic force in the release structure. The initial rotation angle around the X-axis was 0.493°, and the rotation angle during the landing process was between −0.16° and 0.5°. The initial rotation angle around the Y-axis was 0.0138°, and the rotation angle during the landing process was between −0.23° and 0.06°. Lastly, the rotation angle around the Z-axis was between −0.5° and 0.15°; it showed a clockwise rotation trend first and then a counterclockwise rotation trend, reaching a 0.148° rotation change after complete release, which indicated that the carrier was subjected to irregular thrust inside the release structure.

Further, to study the motion details of the carrier landing process deeply and make a reasonable judgment on the stability of the unlocking device of the release structure, statistical data on the motion velocity, angle, and angular velocity changes between the front and rear frames of the carrier were obtained. In addition, the quantitative indicators of the movement of the carrier inside and outside the release structure and the whole process of the release structure were statistically analyzed to achieve a more reliable evaluation basis for the release structure. The statistical data on the quantitative indicators are shown in Figs. 17–19.

Based on the statistical results of the inter-frame motion state indicators, it could be concluded that during the landing process, the velocity of the carrier along the X- and Z-axis was relatively stable. The absolute value of the rotation velocity in the X-axis direction was within 18 mm/s, and the absolute value of the rotation velocity in the Z-axis direction was within 4 mm/s, indicating that there was basically no velocity change in the X- and Z-axis directions between the frames. The frame-to-frame velocity of the carrier along the Y-axis changed incrementally, and there was an acceleration of 0.014 m/s^2. The calculation results obtained from statistical velocity data indicated an unbalanced force on the carrier when the release structure triggered the release. Moreover, since the carrier was received inside the release structure, the carrier rotated irregularly due to the thrust. After it was completely separated from the release structure, its angle change was relatively stable. The rotation angle change along the X and Z axes was within 0.15°, and that along the Y-axis was 0.33°, indicating that the force acting on the carrier in the Y-axis direction was greater than those acting in the X- and Z-axis directions. The angular accelerations along the Y-, X-, and Z-axis directions were −0.00659 rad/s^2, −0.08907 rad/s^2, and 0.03520 rad/s^2, respectively.

According to the quantitative statistical results of the movement index of the carrier in the release structure, complete release, and overall stage, the average, minimum, and maximum values of the movement index of the carrier in the release structure were the highest among the three stages. The movement change range along the Y-axis was wider than those along the X and Z-axes.

In terms of the velocity, the comprehensive velocity inside the release structure showed a counterclockwise rotation trend at a velocity of 206.1952 mm/s, and the external rotation was counterclockwise at a velocity of 312.2681 mm/s; the maximum comprehensive velocity had a counterclockwise rotation trend at a velocity of 439.0490 mm/s. The velocity of the carrier increased and changed, but the velocity changes were most obvious in the Y-axis direction.

In terms of angles, the mean values of the comprehensive angles in the interior, exterior, and overall stages of the release structure were 0.39°, 0.21°, and 0.25°, respectively, and the maximum changes were

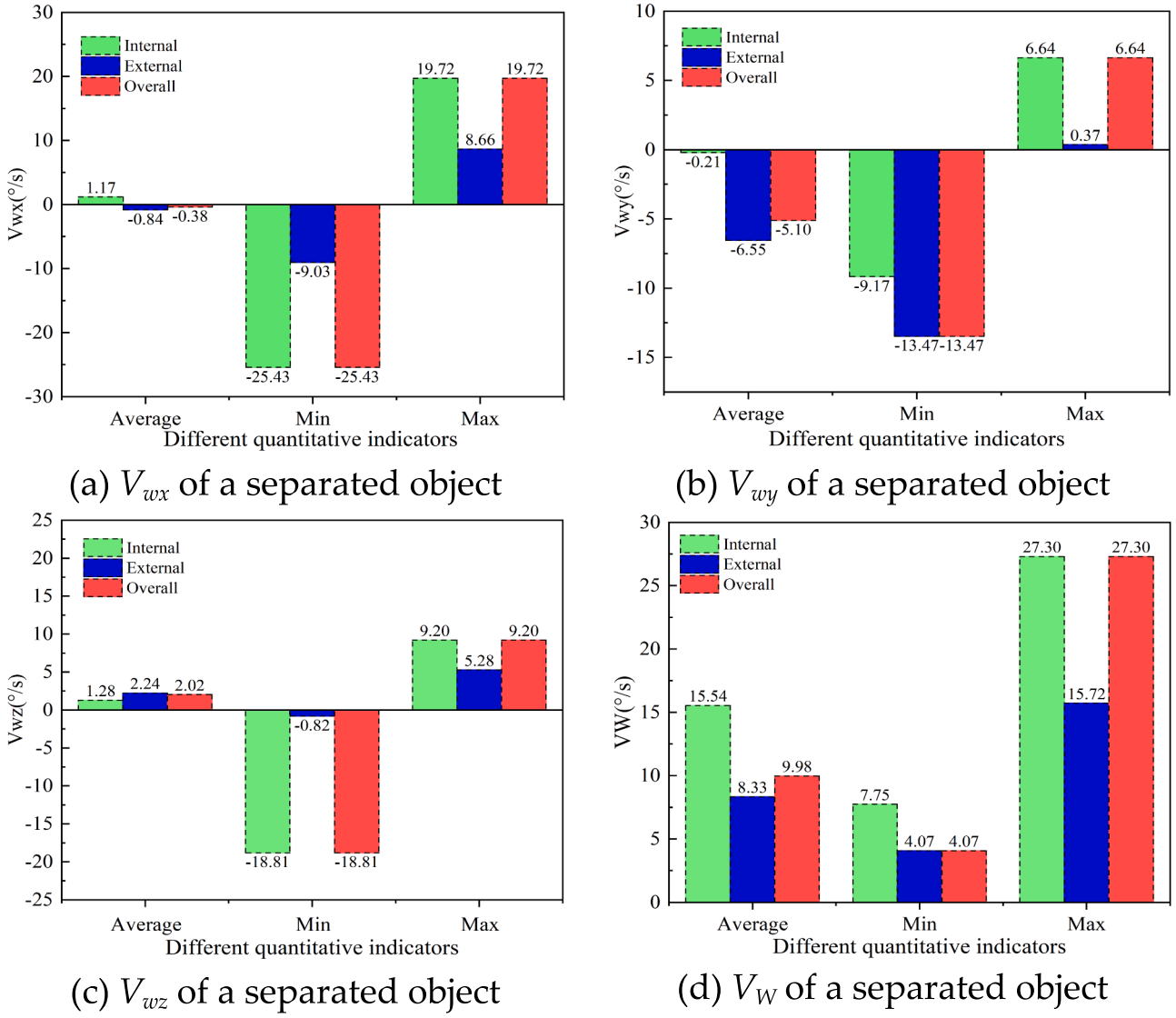

Fig. 19. The angular velocity index statistics of the carrier at different stages: (a)–(c) the angular velocity components on the *X*,*Y*, and *Z* axes, respectively; (d) the comprehensive angular velocity. The horizontal axis shows the average, minimum, and maximum values of the rotational angular velocity of the carrier in different intervals, and the vertical axis represents the angular velocity value.

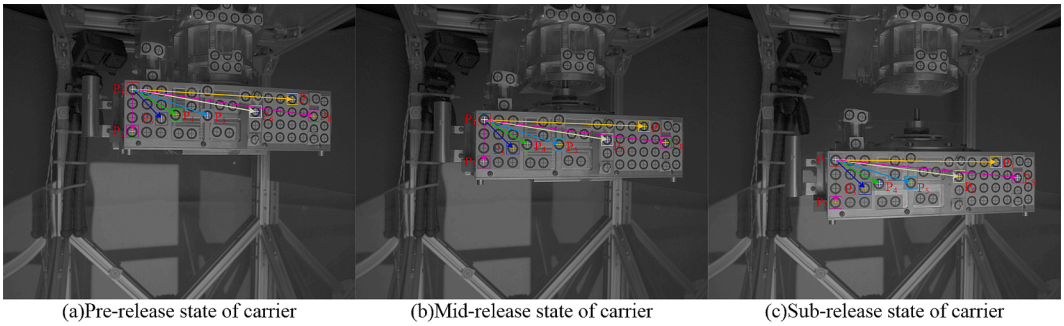

Fig. 20. The schematic diagram of the checkpoint distance distribution; squares of different colors denote different checkpoints; yellow "+" represents the center of the target circle, and red numerals denote the numbers of feature checkpoints; P_1 is the reference point, and the seven connecting lines between each of checkpoints P_2–P_8 and point P_1 are the point distance reference lines.

0.68°, 0.39° and 0.68°, respectively. This indicated that the change range of the carrier inside the release structure was larger than that outside the release structure. When fully released, the motion state was relatively stable, and the angular velocity and angle change had a linear relationship. This indicated that the trigger device performance of the release structure was influenced by the external force to a certain extent, and the ideal no-force state could not be achieved; thus, the trigger performance of the device needs to be further optimized.

Table 6
Statistics on the distance between checkpoints in the three groups of separation experiments.

Checklines	DBC-Num1 (mm)	DBC-Num2 (mm)	DBC-Num3 (mm)	Max values (mm)	Min values (mm)
P_1-P_2	36.733	36.801	36.751	0.068	0.018
P_1-P_3	34.821	34.816	34.791	0.030	0.005
P_1-P_4	43.624	43.685	43.663	0.061	0.022
P_1-P_5	71.091	71.176	71.136	0.085	0.040
P_1-P_6	116.362	116.413	116.391	0.051	0.022
P_1-P_7	152.440	152.465	152.403	0.062	0.025
P_1-P_8	179.366	179.459	179.454	0.093	0.005

3.5. Proposed method stability assessment

Next, to verify the stability and reliability of the proposed method, three sets of experiments on moving carrier separation were performed, and the moving state of the carrier was precisely measured. First, in the landing sequence images of the carrier, the images of three stages of the carrier, namely pre-release, mid-release, and sub-release stages, were selected as test data. Then, eight common checkpoints evenly distributed in all cooperative target circles in the three images were selected as distance verification samples, and the 3D coordinate reconstruction of the checkpoints was completed. Finally, distances of the seven lines connecting each of checkpoints P_2–P_7 and point P_1 were calculated, and the maximum and minimum values of their distance differences in the three groups of separation experiments were determined to evaluate the stability of the measurement system. The sequence image samples and the checkpoint distance distribution are shown in Fig. 20.

By using statistics on the average distance between the checkpoints in the three sets of sequence images, the distance between checkpoints (DBC) and the maximum and minimum values of distance differences were obtained, as shown in Table 6.

The statistical results in Table 6 show that the distance measurement results of the seven checklines obtained using eight public checkpoints were stable, and the maximum distance difference between the checklines was that between points P_1 and P_8, which equaled 0.098 mm. The reason for the analysis was that the distance between points P_1 and P_8 was the farthest, and when the carrier was released, the distance measurement error was relatively large due to the rotation. The minimum distance difference between the checklines was 0.005 mm, and the distance difference values were all less than the point 3D reconstruction accuracy of 0.14 mm, indicating that the point spacing measurement results did not change. This result fully demonstrated that the proposed measurement method had high precision, good stability, and strong reliability and thus could provide reliable technical support for the carrier attitude measurement tests in deep space exploration. Meanwhile, the performance evaluation of the controller could also have a certain reference value.

4. Conclusion

This study proposes a method for accurate measurement of the motion state of a vehicle in a microgravity environment. First, to simulate a microgravity environment in deep space, a high-precision microgravity measurement platform is constructed, and the control interface is designed to obtain two sets of stereo-camera data to perform synchronous imaging of the carrier. Moreover, a self-checking calibration model with additional constraints is developed for camera calibration; this model can provide high-precision time reference and space reference for experiments. Then, the image processing and RANSAC methods are employed to obtain the center coordinates and 3D coordinates of the target circle, and the IMU and binocular vision are integrated to develop a carrier motion state measurement model to ensure the acquisition of motion state indicators with high precision, strong robustness, and good stability. Finally, the movement state indicators of the carrier in the internal, external, and overall areas of the release structure are analyzed, and the control device of the release structure is objectively evaluated.

The novelty of this study and the main conclusions drawn based on the test results of the proposed method are as follows:

(1) A camera calibration method with additional constraints is proposed, and the LM method is used to solve the global optimal calibration parameters rapidly. The number of iterations is controlled to five, and the calibration errors of the two groups of stereo cameras are (0.305, 0.324) pixels and (0.379, 0.255) pixels, which provides a high-precision benchmark for motion state measurement;
(2) The image processing method and the RANSAC method are used to fit the center of the circle, and the fitting error is less than 0.2 pixels. Further, triangulation encryption and various feature constraints are combined to perform dense matching of the same-name points and 3D coordinate reconstruction. The reconstruction accuracy is 0.379 pixels, which ensures both accuracy and stability of the carrier's pose change parameters;
(3) By combining the IMU and stereo vision methods for the pose measurement, the measurement error of the motion state caused by the external force interference can be mitigated, and the measurement accuracy of the carrier's velocity, angle, and angular velocity of better than 0.19 mm/s, 0.09°, and 0.127°/s, respectively, can be ensured. In this way, accurate motion state indicators can be effectively obtained;
(4) The proposed motion state estimation method can reliably evaluate the control performance of the released structure.

Considering the problem of carrier attitude estimation in deep space exploration, this paper proposes a measurement method that combines stereo vision and IMU. Compared to the traditional pose measurement methods, the proposed method has the advantages of a simple structure, high measurement accuracy, and good stability. In addition, it has a certain reference value for the pose control of the carrier and the control performance evaluation of the controller in deep space exploration. Finally, in the field of multi-sensor fusion positioning, the proposed method provides the possibility for vision-assisted positioning technology for scenes where the GNSS signal is out of lock and cannot be located.

In the future research plan, the author will continue to study the precise control of the attitude of the craft into the space environment, and the automatic control of the interactive docking between space stations in the space movement environment. However, the proposed method has certain shortcomings. the on-orbit calibration problem needs to be studied further. In addition, the test presented in this study uses cooperative targets for feature point extraction. Therefore, the case of point sparsity requires further research on automated measurement techniques, which could be part of future work.

CRediT authorship contribution statement

Mingyue Liu: Conceptualization, Methodology, Software, Writing – original draft. **Huizhong Zhu:** Data curation, Writing – original draft.

Xinchao Xu: Writing – review & editing, Investigation. **Youqing Ma:** Conceptualization, Methodology, Supervision. **Shuo Zhang:** Software, Validation. **Junbiao Wang:** Data curation, Resources.

Declaration of Competing Interest

The authors declare that they have no known competing financial interests or personal relationships that could have appeared to influence the work reported in this paper.

Data availability

Data will be made available on request.

Appendix A. Supplementary material

Supplementary data to this article can be found online at https://doi.org/10.1016/j.measurement.2023.113500.

References

[1] H. Wang, D. Hong, C. Liu, M. Piao, Modeling and efficiency analysis for intelligent weapon equipment support system, Journal of Astronautics. 44 (2023) 197–207.
[2] J. Zhao, C. Yang, Non-cascade dual-rate composite decentralized operational optimal control for complex industrial processes, Acta Autom. Sin. 49 (2023) 172–184.
[3] L. Zhou, Z.-Q. Li, H. Yang, Y.-T. Fu, H. Wang, Data-driven integral sliding mode control based on disturbance decoupling technology for electric multiple unit, J. Franklin Inst. (2023), https://doi.org/10.1016/j.jfranklin.2023.07.005.
[4] A. Wang, Analysis of the development and application situation of artificial intelligence for intelligent manufacturing, AI-View. 32 (2023) 1–7.
[5] H. Zhou, Y. Hao, Dynamic state feedback control for heading motion of AUV, Aerospace Control and Application. 29 (2022) 2244–2249.
[6] B. Li, Y. Yu, S. Wang, Spacecraft power-optimal attitude control using control momentum gyroscopes, Aerospace Control and Application. 49 (2023) 30–39.
[7] C. Yang, W. Lu, Y. Xia, Reliability-constrained optimal attitude-vibration control for rigid-flexible coupling satellite using interval dimension-wise analysis, Reliab. Eng. Syst. Saf. 237 (2023), 109382, https://doi.org/10.1016/j.ress.2023.109382.
[8] M.N. Hasan, M. Haris, S. Qin, Fault-tolerant spacecraft attitude control: A critical assessment, Prog. Aerosp. Sci. 130 (2022), 100806, https://doi.org/10.1016/j.paerosci.2022.100806.
[9] C. Yang, Y. Xia, Interval uncertainty-oriented optimal control method for spacecraft attitude control, IEEE Trans. Aerosp. Electron. Syst. (2023) 1–13, https://doi.org/10.1109/TAES.2023.3257777.
[10] N. Yefymenko, R. Kudermetov, Quaternion models of a rigid body rotation motion and their application for spacecraft attitude control, Acta Astronaut. 194 (2022) 76–82, https://doi.org/10.1016/j.actaastro.2022.01.029.
[11] Y. Duan, L. Guan, High precision attitude measurement and calibration method of spacecraft based on precision star sensor, Computer Measurement & Control. 27 (2019) 1–5.
[12] C. Yang, W. Lu, Y. Xia, Uncertain optimal attitude control for space power satellite based on interval Riccati equation with non-probabilistic time-dependent reliability, Aerosp. Sci. Technol. 139 (2023), 108406, https://doi.org/10.1016/j.ast.2023.108406.
[13] Y. Wang, F. Yuan, Novel camera calibration method based on cooperative target pose measurement, Acta Opt. Sin. 36 (2016) 180–188.
[14] Z. Wei, G. Feng, D. Zhou, et al., A review of position and orientation visual measurement methods and applications, Laser & Optoelectronics Progress. 60 (2023) 144–176.
[15] X. Wang, B. Fan, T. Pan, et al., Research on laser tracking measurement method for target dynamic pose, Bulletin of Surveying and Mapping. 207 (2016) 210–221.
[16] X. Yang, H. She, H. Li, et al., Attitude estimation of non-cooperative spacecraft based on deep learning, Navigation Positioning and Timing. 8 (2021) 90–97.
[17] M. Tao, Y. Yao, H. Yuan, et al., Visual target design and pose measurement method for UAV autonomous landing, Chinese Journal of Scientific Instrument. 43 (2022) 155–164.
[18] G. Huang, G. Li, B. Wang, S. Ye, Evolution for monocular vision measurement, Acta Metrologica Sinica. 4 (2004) 314–317.
[19] L. Xu, Q. Fu, W. Tao, et al., Monocular vehicle pose estimation based on 3D model, Opt. Precis. Eng. 29 (2021) 1346–1355.
[20] J. Zhang, W. Lan, Z. Jin, et al., A continuous attitude measurement method of three-axis air bearing platform based on close range photogrammetry, Journal of Navigation and Positioning. 8 (2020) 69–75.
[21] J. Lei, Research on single-station measurement and estimationmethod of target axial attitude based on the moving platform, University of Chinese Academy of Sciences (2022).
[22] H. Gómez Martínez, G. Giorgi, B. Eissfeller, Pose estimation and tracking of non-cooperative rocket bodies using Time-of-Flight cameras, Acta Astronaut. 139 (2017) 165–175, https://doi.org/10.1016/j.actaastro.2017.07.002.
[23] Z. Sun, Y. Gao, Relative position and attitude measurement for non-cooperative spacecraft based on binocular vision, Journal of Astronautic Metrology and Measurement 37 (2017) 1–6.
[24] X. Gao, J. Yu, M. Tan, An Online 3D modeling method for pose measurement under uncertain dynamic occlusion based on binocular camera, Sensors 23 (2023).
[25] X. Kang, D. Yao, Attitude measurement for relative object based on binocular vision, Missiles and Space Vehicles. 330 (2014) 82–86.
[26] F. Yin, W. Chou, Y. Wu, G. Yang, S. Xu, Sparse unorganized point cloud based relative pose estimation for uncooperative space target, Sensors 18 (2018) 1009.
[27] K. Yan, Researchon LaserTracking Attitude Measurement Method based on PSD and Monocular Vision, Hubei University of Technology, 2020.
[28] L. Zhang, Z. Xiong, W. Feng, W. Zhou, D. Dong, Laser tracking attitude angle measurement method based on vision and laser collimation, Chinese Journal of Scientific Instrument. 41 (2020) 30–36.
[29] H. Xu, Z. Xiong, L. Zhang, W. Feng, Z. Zhai, W. Zhou, D. Dong, Laser tracking attitude angle measurement method based on weighted least squares, Infrared and Laser Engineering. 6 (2022) 353–358.
[30] K. Li, H. Zhang, C. Hu, Learning-Based Pose Estimation of Non-Cooperative Spacecrafts with Uncertainty Prediction, Aerospace 9 (2022) 592.
[31] H. Han, H. Kim, H. Bang, Monocular Pose Estimation of an Uncooperative Spacecraft Using Convexity Defect Features, Sensors 22 (2022) 8541.
[32] X. Liu, H. Wang, X. Chen, W. Chen, Z. Xie, Position Awareness Network for Non-Cooperative Spacecraft Pose Estimation Based on Point Cloud, IEEE Trans. Aerosp. Electron. Syst. 1–13 (2022).
[33] L. Deng, H. Suo, Y. Jia, C. Huang, Pose Estimation Method for Non-Cooperative Target Based on Deep Learning, Aerospace 9 (2022) 770.
[34] L. Zhang, H. Shang, Y. Lin, A Novel Distribution for Representation of 6D Pose Uncertainty, Micromachines 13 (2022) 126.
[35] Z.C. Shi, Y. Shang, X.F. Zhang, G. Wang, DLT-Lines Based Camera Calibration with Lens Radial and Tangential Distortion, Exp. Mech. 61 (2021) 1237–1247, https://doi.org/10.1007/s11340-021-00726-5.
[36] S. Zhang, Y.Jia, S. Peng, et al. Self-calibration of the stereo vision system of the Chang'e-4 Lunar rover based on the points and lines combined adjustment. Photogrammetric Engineering & Remote Sensing. 86(2020) 169-176.—开始公式.
[37] Y. Ma, Y. Jia, S. Liu, Y. Jia, Bundle Adjustment Based on LMAlgorithm for RoverNavigation and Localization. Journal of Northeastern University(Natural Science). 35(2014) 489-493.
[38] S. Zhang, S. Liu, Y. Ma, C. Qi, H. Ma, H. Yang, Self calibration of the stereo vision system of the Chang'e-3 lunar rover based on the bundle block adjustment, ISPRS J. Photogramm. Remote Sens. 128 (2017) 287–297, https://doi.org/10.1016/j.isprsjprs.2017.04.004.
[39] S. Nagai, I. Yoshida, K. Oshiro, R. Sakakibara, Acceleration of surface roughness evaluation using RANSAC and least squares method for Running-in wear process analysis of plateau surface, Measurement 203 (2022), 111912, https://doi.org/10.1016/j.measurement.2022.111912.
[40] X. Xu, X. Li, Y. Xu, et al., A Real-Time Cross-Lens Continuous Tracking Method for Vertical Mounted Cameras, Geomatics and Information Science of Wuhan University. 46 (2021) 1247–1258.
[41] Y. Lv, W. Liu, W. Du, Further Study and Application for One-Dimensional Homography Matrix, Acta Opt. Sin. 38 (2018) 216–222.
[42] P. Zhang, Y. Wu, Q. Cai, Improved solution for relative pose based on homography matrix. Computer Engineering and Applications. Computer Engineering and Applications. 53(2017) 25-30.
[43] C. Z, B. Fan, L. Tian, et al. Statistical optimization feature matching algorithm based on epipolar geometry. Acta Aeronautica et Astronautica Sinica. 39(2018) 163-171.
[44] C. Lai, Study on Dense Matching Method For Close-Range Stereo Image, Nanjing Normal University, 2012.
[45] D. Kim, H. Jang, I. Kim, et al. Proceedings of the IEEE/CVF Conference on Computer Vision and Pattern Recognition (CVPR). (2023) 5023-5032.
[46] T. Luhmann, S. Robson, S. Kyle, J. Boehm, Close-Range Photogrammetry and 3D Imaging, Walter de Gruyter, 2013.
[47] Y. Guo, Z. Li, H. He, et al., A squared Msplit similarity transformation method for stable points selection of deformationmonitoring network, Acta Geodaetica et Cartographica Sinica. 49 (2020) 1419–1429.
[48] Y. Ma, S. Liu, Q. Li, An advanced multiple outlier detection algorithm for 3D similarity datum transformation, Measurement 163 (2020), 107945, https://doi.org/10.1016/j.measurement.2020.107945.
[49] J. Shang, C. Liu, H. Shi, et al., Indoor single-star positioning method based on IMU assisting, Journal of Chinese Inertial Technology. 25 (2017) 636–6426.
[50] Y. Jiang, S. Li, G, Yan, et al. Vehicle navigation information extraction method based on dual-axis rotation-modulationinertial measurement. Journal of Chinese Inertial Technology. 30(2022) 304-308.
[51] Z. Wang. D. Li, S. Zhao, et al. Using position and velocity of three points to calculate attitude parameters of SINS. Journal of Navigation and Positioning. 10 (2022) 10-17.
[52] X. Xu, M. Liu, S. Peng, Y. Ma, H. Zhao, A. Xu, An in-orbit stereo navigation camera self-calibration method for planetary rovers with multiple constraints, Remote Sens. (Basel) 14 (2022) 402.
[53] D.B. Gennery, Generalized camera calibration including fish-eye lenses, Int. J. Comput. Vis. 68 (2006) 239–266.
[54] B. Caprile, V. Torre, Using vanishing points for camera calibration, Int. J. Comput. Vis. 4 (1990) 127–139.
[55] V. Mahboub, On weighted total least-squares for geodetic transformations, J. Geod. 86 (2011) 359–367.